GLOBAL NUMERICAL MODEL FOR THE EVALUATION OF THE GEOMETRY AND OPERATION CONDITION EFFECTS ON HOLLOW CATHODE INSERT AND ORIFICE REGION PLASMAS

by

Oğuz Korkmaz

B.S., Mechanical Engineering, Yıldız Technical University, 2013

Submitted to the Institute for Graduate Studies in
Science and Engineering in partial fulfillment of
the requirements for the degree of
Master of Science

Graduate Program in FBE Program for which the Thesis is Submitted

Boğaziçi University

2015

GLOBAL NUMERICAL MODEL FOR THE EVALUATION OF THE GEOMETRY
AND OPERATION CONDITION EFFECTS ON HOLLOW CATHODE INSERT
AND ORIFICE REGION PLASMAS

APPROVED BY:

Assist. Prof. Murat Çelik   . . . .
(Thesis Supervisor)

Assoc. Prof. Kunt Atalık   . . . .

Assist. Prof. Ahmet Öncü   . . . .

DATE OF APPROVAL: 27.January.2015

ACKNOWLEDGEMENTS

ABSTRACT

GLOBAL NUMERICAL MODEL FOR THE EVALUATION OF THE GEOMETRY AND OPERATION CONDITION EFFECTS ON HOLLOW CATHODE INSERT AND ORIFICE REGION PLASMAS

Thermionic hollow cathodes have been widely used in wide variety of areas such as spacecraft electric propulsion systems, material processing and lasers for more than half a century as efficient electron sources. Especially in electric propulsion systems, hollow cathodes are being used as electron sources for propellant ionization and ion beam neutralization. Moreover, hollow cathode is also a promising candidate for utilization as a stand-alone propulsion system in microsatellites or nanosatellites due to its small physical size, low power consumption and ease of operation. On the other hand, the small geometry of the typical orificed hollow cathodes make the plasma diagnostics difficult which is why numerical studies become important for understanding the driving physical processes behind their operation, and the effects of the geometry and the operation parameters on cathode performance. In this thesis a global numerical model for the insert and orifice plasma of a hollow cathode is presented where volume averaged plasma parameters are considered for both regions. The results of this study show that the developed model can be used for designing and sizing orificed hollow cathodes as comparisons with the results of experimental and other numerical studies are in good agreement with the ones obtained from the developed model.

ÖZET

GEOMETRİ VE ÇALIŞMA KOŞULLARININ OYUK KATOT YAYICI VE ORİFİS PLAZMA BÖLGELERİNE OLAN ETKİSİNİN DEĞERLENDİRİLMESİ İÇİN GLOBAL NÜMERİK MODEL

Termiyonik oyuk katotlar uzay araçlarının elektrik itki sistemleri, malzeme işlenmesi ve lazerler gibi bir çok alanda yarım yüzyılı aşkın bir süredir etkin elektron kaynakları olarak kullanılmaktadırlar. Oyuk katotlar özellikle elektrik itki sistemlerinde yakıtın iyonlaştırılması ve iyon demetinin nötürleştirilmesinde kullanılmaktadırlar. Ayrıca oyuk katot küçük fiziksel boyutu, düşük güç tüketimi ve kullanım kolaylığı sayesinde mikro ve nano uydularda kendi başına itki sistemi olarak kullanılmak için umut vadedici bir adaydır. Öte yandan oyuk katotların küçük bir geometriye sahip olmaları plazma ölçümlerini zorlaştırmaktadır. Bu sebepten ötürü, bu cihazın çalışmasının ardında yatan temel fiziksel prensiplerin ve de geometri ve çalışma koşullarının katot performansı üzerindeki etkilerinin anlaşılabilmesi için, nümerik çalışmalar önem arz etmektedir. Bu tez çalışmasında, yayıcı ve orifis bölgelerindeki plazma parametrelerinin düzgün dağılımlı olduğu kabul edilerek oyuk katodun söz konusu bölgeleri için global bir nümerik model geliştirilmiştir. Geliştirilen modelden elde edilen sonuçların literatürdeki diğer nümerik ve deneysel çalışmaların sonuçları ile iyi derecede uyumlu olması, bu modelin orifisli oyuk katotların dizaynında ve boyutlandırlmasında kullanılabilir olduğunu göstermektedir.

TABLE OF CONTENTS

LIST OF FIGURES

LIST OF TABLES

LIST OF SYMBOLS

A	Richardson constant
A_{emit}	Insert effective emission area
D	Thermionic emitter material constant
d_o	Orifice diameter
E_s	Electric field of the cathode sheath
h	Planck's constant
$I_{Bohm,orf}$	Bohm ion current at the orifice sheath edge
I_{em}	Thermionic electron emission current
I_d	Discharge current
I_i	Ion current towards the insert surface
$I_{i,out}$	Ion current out of the control volume
I_r	Random electron current towards insert surface
$I_{r,orf}$	Random electron current towards orifice surface
$J_{i,Bohm}$	Bohm ion current density at the sheath edge
$J_{i,th}$	Ion thermal current density
k_B	Boltzmann's constant
L_{emit}	Insert effective emission length
L_o	Orifice length
$\dot{m}$	Propellant mass flow rate in kg/s
m_e	Electron mass
m_i	Ion mass
N_e	Neutral number density of insert plasma
N_o	Neutral number density of orifice plasma
n_e	Insert plasma density
n_o	Orifice plasma density
P	Neutral particle pressure
Q	Propellant mass flow rate in sccm
q	Electron charge

R_e	Insert plasma resistance
R_g	Universal gas constant
R_o	Orifice plasma resistance
r_e	Insert radius
r_o	Orifice radius
$T_{e,ins}$	Insert plasma electron temperature in K
$T_{eV,ins}$	Insert plasma electron temperature in eV
$T_{e,orf}$	Orifice plasma electron temperature in K
$T_{eV,orf}$	Orifice plasma electron temperature in eV
$T_{i,orf}$	Orifice plasma ion temperature in K
$T_{iV,orf}$	Orifice plasma ion temperature in eV
$T_{w,ins}$	Insert wall temperature
$T_{w,orf}$	Orifice wall temperature
U_i	First ionization energy of propellant
W	Evaporation rate of insert material
γ	Specific heat ratio of propellant
ϵ_0	Permittivity of free space
ζ	Viscosity
η	Plasma resistivity
Λ	Coulomb logarithm
λ_{01}	The first zero of zeroth order Bessel function of the first kind
ν_{ei}	Electron ion collision frequency
ν_{en}	Electron neutral collision frequency
σ_{cex}	Resonant charge exchange collision cross section
σ_{en}	Electron neutral collision cross section
ϕ_{eff}	Insert effective work function
ϕ_s	Sheath potential
$\phi_{s,orf}$	Orifice sheath potential
ϕ_{wf}	Insert work function

LIST OF ACRONYMS/ABBREVIATIONS

CAD	Computer Aided Drawing
HC	Hollow Cathode
OHC	Orificed Hollow Cathode
PIC	Particle In Cell
RF	Radio Frequency

1. INTRODUCTION

Thermionic hollow cathodes are being used in wide-variety of applications as efficient electron sources. Ion and Hall thrusters require a particular device that can provide electrons which are necessary for the ionization of the neutral propellant atoms and neutralization of the ion beam leaving the thruster to avoid spacecraft charging. Therefore, a specific component, such as a hollow cathode or in some other applications a heated thermionic emitter wire [1, 2] must be added to thruster assembly to satisfy the electron current requirement.

In early applications of ion thrusters, heated tungsten filaments was used as electron source. It was necessary to operate the filaments at temperatures as high as 2600 K in order to obtain electron current densities about 1 A/cm^2. Operating at such high temperatures requires large amount of heat power which significantly reduces the efficiency of the system. In addition, lifetime of tungsten filaments was limited due to high operation temperatures which also limits the time of the space missions.
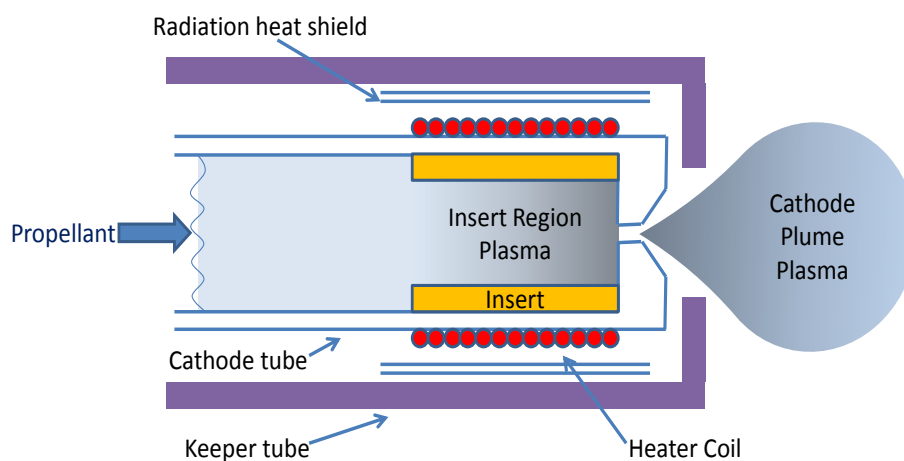
Figure 1.1. Schematic of a hollow cathode.

Tungsten originated problems eliminated by the development of hollow cathodes. Orificed hollow cathodes (OHCs) that are used in electric propulsion systems typically consist of a thin, long, hollow cylindrical refractory metal tube in which an insert material with low work function is placed. A schematic of a hollow cathode is shown in Figure 1.1.

Even tough an elaborate discussion of the parts and operation of hollow cathode is given in the following sections, it is worthwhile to give a brief summary of the parts of hollow cathode assembly. Three main parts of an OHC are insert, orifice and keeper. Insert region is where emitter material is placed. The ease of electron release from emitter material with thermionic emission determines the power consumption and operation parameters of hollow cathode. Barium-Oxide impregnated tungsten ($BaO - W$), lanthanum hexaboride (LaB_6) and cerium hexaboride (CeB_6) are the most common materials used as thermionic emitter in OHC [3]. $BaO - W$ has work function around 1.6 eV [4] and can provide sufficient electron current density under $1000°$C. However, this material can easily be poisoned by impurities in the propellant gas, causing its work function to increase dramatically. For this reason, high purity propellant usage has an extreme importance to ensure high lifetime in $BaO - W$ OHC. LaB_6, on the other hand, is resistant against poisoning and also has low evaporation rate which makes it a suitable material for long lifetime hollow cathodes [5]. The work function of this material is around 2.67 eV [4]. Due to the fact that LaB_6 has higher work function than $BaO - W$ material, it requires higher temperature to provide same amount of current density. LaB_6 reacts with many refractory materials such as molybdenum. Therefore, extreme attention should be paid for selection of supportive material of LaB_6. For a review of various thermionic emitter materials, the reader should look at Section 1.2.

Orifice, a refractory metal, is typically welded at the downstream end of the tube. The reason for orifice utilization in OHC is to maintain high internal pressure, on the order of 10^3 - 10^4 Pa. Moreover, orifice also contributes to heating of the emitter material.

Cathode tube is enclosed with a cylindrical tube named as keeper tube. Keeper provides an electric potential difference in order to attract the electron in the orifice and insert region plasmas. Another task of the keeper tube is to prevent the cathode from ion bombardment coming from thruster plasma.
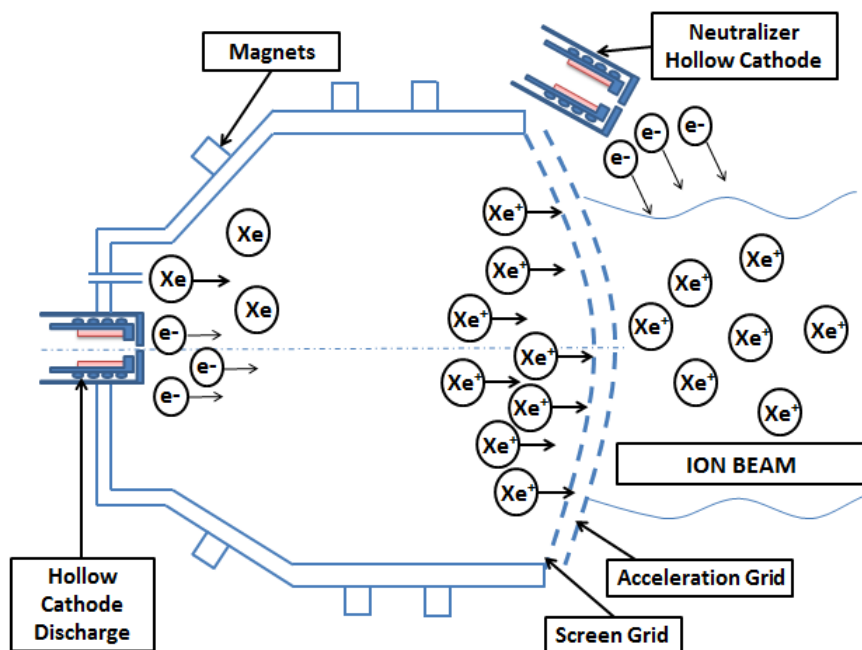
Figure 1.2. Schematic of a typical ion thruster.

1.1. Hollow Cathode Applications in Electric Propulsion

1.1.1. Ion Thrusters

A Kaufman type ion thruster employs two hollow cathodes. One of the hollow cathodes emits electrons which are necessary for the ionization of the propellant atoms inside the discharge chamber of the ion thruster. Figure 1.2 shows the structure of a Kaufman type ion thruster. Another one is used to neutralize the ion beam expelled out of the ion thruster. The neutral propellant atoms (mostly xenon atoms) are injected into the discharge chamber of the ion thruster. The discharge chamber is a cylindrical shaped anode which also houses the centrally mounted hollow cathode. Magnetic field is also applied in order to increase the length of the trajectory of electrons. Increasing the length of the trajectory of electrons in discharge chamber leads to higher collisions and therefore makes ion thruster more efficient. Generated ions in ionization chamber are then accelerated by grids at the downstream end. The grids are biased at different potentials. These expelled ions are then neutralized by the electrons emitted from an external hollow cathode. Neutralization of the ion beam is necessary to prevent spacecraft charging.
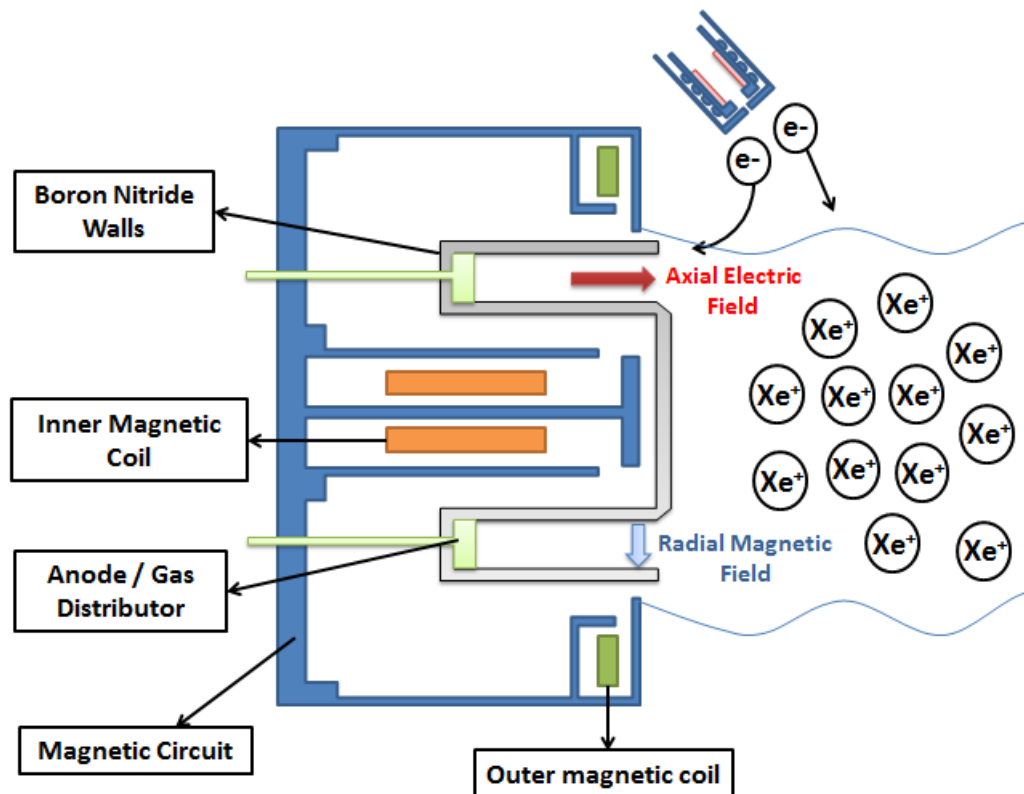
Figure 1.3. Schematic of a typical Hall effect thruster.

1.1.2. Hall Thrusters

The hollow cathode used in a Hall effect thruster works as both the discharge cathode and the neutralizer cathode. Mostly only one hollow cathode is used in a single-stage Hall thruster. A schematic of a typical Hall effect thruster can be seen in Figure 1.3. The working principle of Hall effect thrusters is to ionize the propellant and accelerate the charged particles to obtain thrust. Inner and outer electromagnets are used to create radial magnetic field. The electrons emitted from the hollow cathode are accelerated towards anode by the applied high voltage between anode and external hollow cathode. These electrons begin to spiral in the direction perpendicular to the applied magnetic field and electric field. When the propellant atoms are injected, they collide with these electrons and as a consequence, ions are created. The ions are then accelerated along the axial electric field. The ions expelled out of the thruster are neutralized by the electrons emitted from the hollow cathode. Erosion of the dielectric walls (boron nitride walls) due to sputtering determines the life of this thruster.

1.2. Hollow Cathode Construction

Generally, a hollow cathode consists of three main sections: emitter, orifice and keeper. A cross-section view of a typical hollow cathode can be seen in Figure 1.4 and a 3D CAD drawing of whole hollow cathode assembly can be seen in Figure 1.5.
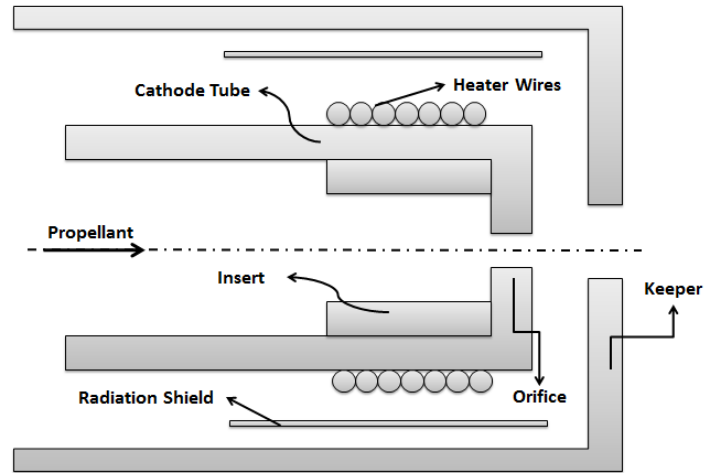
Figure 1.4. Geometry of hollow cathode.
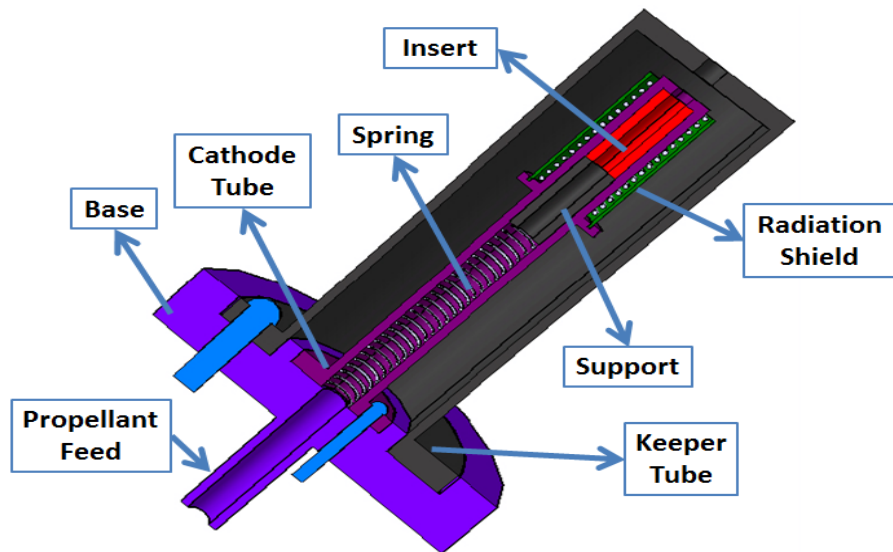
Figure 1.5. 3D CAD drawing of a typical hollow cathode assembly.

Insert material, which emits electrons with thermionic emission, is situated in the emitter region. Heater coils, which are generally made of refractory materials such as tungsten or tantalum, are wrapped around the cathode tube. Electrical current provided to these coils by an external power source supplies resistive heating mechanism.

Rather than direct heating, there are also different methods of heating the thermionic emitter such as radiation heating, combination of radiation and electron heating [6, 7, 8] in different applications. However, sheathed refractory metal wire wrapped around the cathode tube is the most common way of heating in hollow cathodes.

Aside from classical heater design (wrapping sheathed refractory wire around cathode tube), there are also different heater designs in the literature. The heater designed at Massachusetts Institute of Technology [9] has a ceramic tube (boron nitride) with helical grooves. Bare heater wire (instead of a sheathed one) is wrapped in this grooves. 3D CAD drawing of this design can be seen in Figure 1.6. The heater designed at the University of Michigan [10] has horizontal grooves that are machined on boron nitride base. Similarly, bare heater wire is wrapped around these grooves. 3D CAD drawing of this design is given in Figure 1.7.
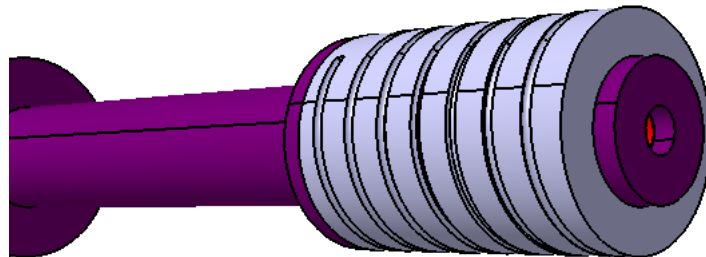
Figure 1.6. Courtney's heater design [9].
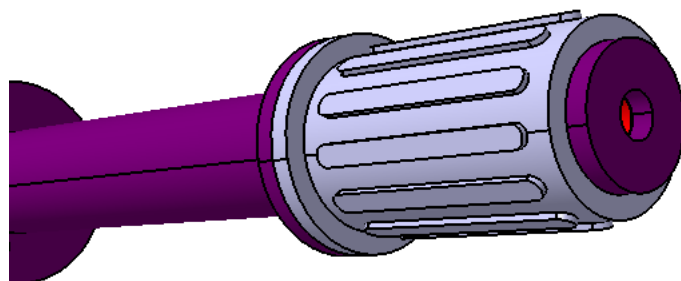
Figure 1.7. Heater design of University of Michigan [10].

The task of heater coils is to supply enough amount of heat to release sufficient level of thermionic electron emission from insert. Therefore, utilization of low work function insert is an important parameter to reduce the power consumption of hollow cathode electron sources. In order to minimize heat loss due to radiative heat transfer, a radiation shield is also mounted in the gap between heater coils and keeper tube. After system reaches steady state regime, the heater is turned off. From this point on, the necessary amount of heat, for the continuation of sufficient thermionic electron emission from insert material, is provided by ion and electron bombardment of insert surface, and conduction of heat from orifice [11, 12].

The propellant (generally xenon gas) is injected to the system from the base. Neutral propellant atoms start to experience collisions when they reach emitter region. The electrons, emitted from insert material via thermionic emission, hit the neutral propellant atoms and cause ionization. The plasma created in the emitter region is called insert plasma.

Another part of a typical hollow cathode is the cylindrical keeper tube which is placed around the cathode tube. Main reason for keeper utilization is to create an attracting potential difference for electrons. This potential difference generated by biased keeper tube causes electrons to be extracted out of the cathode tube. At initiation stage, the neutral propellant atoms injected from the upstream end of hollow cathode experience collisions with thermionically emitted electrons when they reach insert region. As a consequence of these collisions between neutral atoms and emitted electrons, a dense plasma is created in the emitter region. After steady state operation is achieved, keeper is used for regulating the electron discharge. Keeper also prevents the cathode assembly from the damage that ion bombardment coming from thruster plasma can cause. Usage of a keeper also helps maintain high insert temperature [13]. The circuit diagram of a typical hollow cathode experimental setup can be seen in Figure 1.8.

Thermionic emitter material plays a significant role on power consumption and operating parameters of hollow cathodes. The first concern of selection of emissive
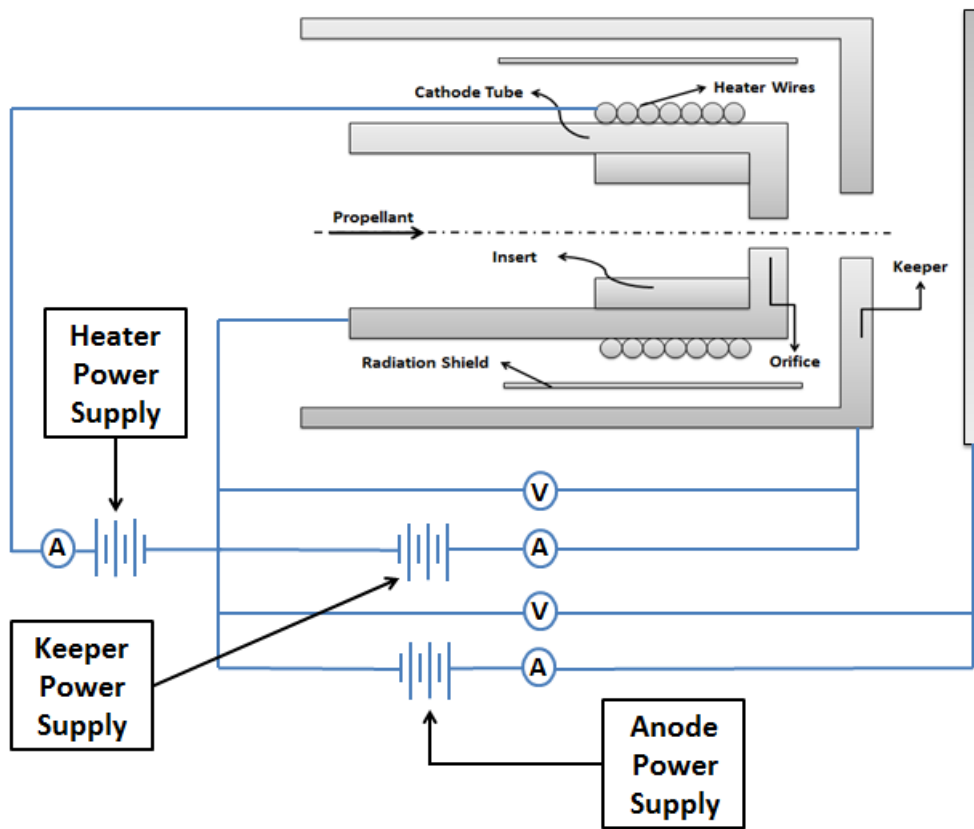
Figure 1.8. Electrical circuit diagram of hollow cathode.

material is that it should have low work function. In other words, it should give high emission current at low temperatures. Low work function, along with evaporation rate and poisoning resistance against the impurities in the propellant are important parameters in emitter material selection. Several materials have been used as insert material. Emission current densities of several thermionic materials with respect to temperature can be seen in Figure 1.9 and evaporation rate of several materials are given in Figure 1.10.

Refractory metal cathodes such as tungsten requires high heater power and have limited lifetimes due to their high evaporation rates. Especially for high electron current demanding applications such as ion sources, plasma generators, ion lasers refractory metal cathodes are not suitable candidates for electron emission. On the other hand, LaB_6 can provide high current densities, low evaporation rates and resistance to poisoning. LaB_6 has a work function of 2.67 eV depending on the surface stoichiometry. LaB_6 can emit 10 A/cm^2 at temperature 1650°C. Unfortunately, LaB_6 can be easily
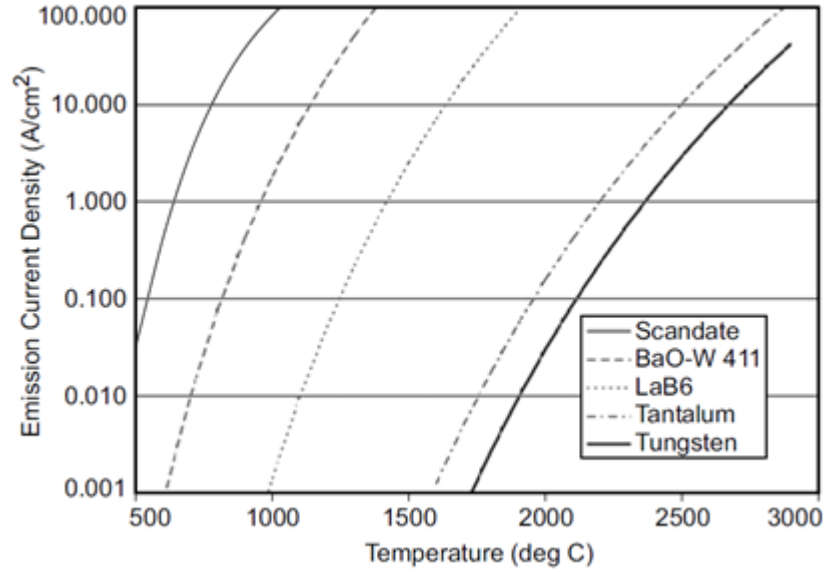
Figure 1.9. Emission current density versus temperature for various cathode materials [11].
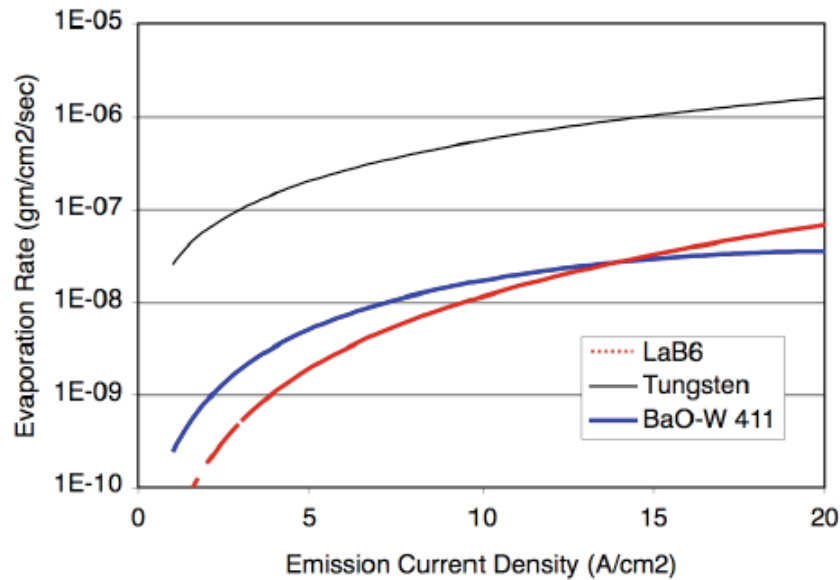
Figure 1.10. Evaporation rate versus emission current density for various cathode materials [14].

fractured by thermal shock in case of heating or cooling rapidly. However, its high thermal conductivity ensures a more uniform temperature distribution on the insert surface [15]. The lanthanum hexaboride thermionic electron emitter was first discovered by Lafferty in 1950s [16] and afterwards studied by several other researches [17, 18]. It is

started to be used in hollow cathodes in 1970s [4]. Hollow cathodes with LaB_6 insert material has a long application history in Russia. Hundreds of LaB_6 cathodes have been used in Russian Hall thrusters [19, 20]. Goebel used LaB_6 cathode for the first time in the United States [15]. The lanthanum boride compounds can be divided into three categories, LaB_4, LaB_6, LaB_9, where their composition can be identified with the surface color. LaB_6 has purple, LaB_4 has grey and LaB_9 has blue surface color [21].

Lanthanum hexaboride is a reactive material with refractory metals such as tungsten. Boron coming from LaB_6 diffuses to the refractory metal, which is used to support LaB_6 in its position, and forms interstitial boron compounds in metal lattices. The boron diffusion embrittles the refractory materials at high temperatures and cause structural failure. Thus, Lafferty [16] states that this material needs to be supported by materials which obstruct diffusion of boron towards the support material. To avoid these negative circumstances, LaB_6 is mostly supported by materials such as carbon, tantalum carbide and rhenium. Tungsten-boron and molybdenum-boron compounds were seen as a thick white powder on the emitter surface when one of them (tungsten or molybdenum) was used to support the LaB_6 [22]. In order to reduce the chemical reactions, rhenium and tantalum carbide can be used as support material.

Rhenium metal has hexagonal closed packed lattice structure which does not allow interstitial diffusion of boron atoms into the lattice which makes it a good support material for LaB_6. Moreover, it has a high melting point of 3180°C and low vapour pressure [23].

Particularly, molybdenum is a poisonous metal to LaB_6 due to the formation of molybdenum borides and thus increase in the work function. The work function of LaB_6 with a clean surface was reported as 2.36 eV and Richardson constant of 120 A/cm^2K^2 [24]. It was seen that the work function of LaB_6 does not change dramatically even though it is exposed to surface impurities which can be considered as an evidence of the fact that LaB_6 can perform well even in poisonous environment [24, 25].

Graphite totally eliminates the problems related to chemical reactions. Graphite has a slightly greater thermal expansion coefficient than LaB_6 and also its electrical contact, mechanical stability is suitable for operation at high temperatures [4, 26]. As a matter of fact whole cathode assembly, especially thermionic emitter and orifice, works at high temperatures (around 1500 K), thermal properties of the materials working together in the assembly is an important parameter. Since thermal properties of certain grades of graphite is similar to those of LaB_6 and it does not react with LaB_6, graphite is a good option to be used as supporting material [22, 26].

Apart from different support materials, different support structure constructions have also been tried in order to eliminate the problems due to chemical reactions. Broers [8] developed a construction in which only some portion of the cathode is heated by a tungsten coil wrapped around. This tungsten coil heater is not in contact with the emitting part of the cathode.

Another emissive material, which does not have as widely usage in hollow cathodes as LaB_6, is CeB_6. The work function of CeB_6 is slightly lower than LaB_6. CeB_6 has a work function of between 2.5-2.62 eV (depending on the surface stoichiometry). At similar current densities, it has a lower evaporation rate in comparison to LaB_6. This emissive material is also resistant against poisoning [27]. This emissive material does not have a long application history in hollow cathodes but preliminary investigations point out that this material is a promising cathode emitter [27].

Another material that can be used as emitter is barium oxide (BaO). These so called "oxide cathodes" or "dispenser cathodes" have work function less than 2 eV and they can produce high current densities. The reason why this type of cathodes are called as dispenser cathodes is that in this configuration, there is a porous matrix which is used as a reservoir for emissive material (barium oxide) that dispenses through the pores on the matrix. There are two groups of dispenser cathodes. The first ones are cavity reservoir dispenser cathodes and the second ones are impregnated dispenser cathodes [28].

Cavity dispenser cathodes which simply consist of thin porous tungsten behind which there is a coating of barium carbonate. The schematic can be seen in Figure 1.11. This cathode is called as L cathode. In this cathode barium dispenses towards the emitting surface through the porous tungsten pores. This L cathode has a low work function of 2 eV [28].
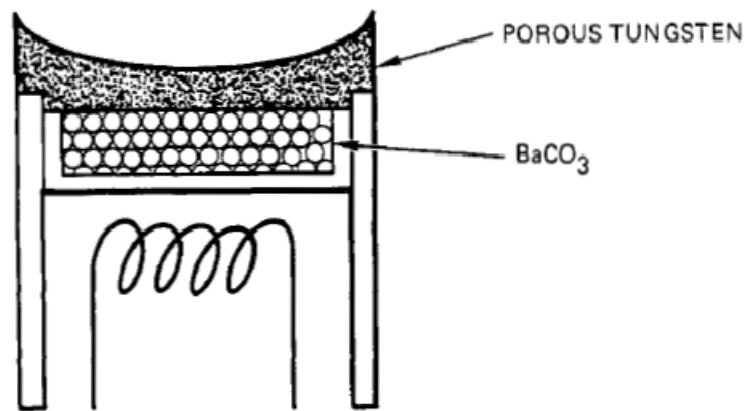
Figure 1.11. L type dispenser cathode [28].

Another example of dispenser cathode, which also falls into cavity reservoir dispenser cathode category, is Metall-Kapillar-Kathoden or MK cathode. MK cathode was developed by Helmet Katz at Siemens in Germany. The construction of MK cathode is similar to L type cathode. MK cathodes have a porous tungsten and a barium reservoir as well. This time the material in reservoir is barium oxide on which a tungsten wool is placed. Tungsten wool over barium oxide accelerates the release of reaction products due to the release of free barium. MK cathodes have two types: osmium coated and uncoated. The work function of uncoated version is nearly that of L cathodes but the coated version is around 1.8 eV. Another cavity reservoir cathode is controlled porosity dispenser (CPD) cathode. CPD cathode was researched at the U.S. Naval Research Laboratory and developed at Varian Associates and Hughes Aircraft Company. In this cathode a thin tungsten foil with a uniform laser drilled holes is used rather than a porous tungsten disk as was the case in previous dispenser cathodes. Barium calcium aluminate compound mixed with tungsten powder 5 micron in diameter is placed in the reservoir. In this design there are no worries of the blockage of pores due to the reaction products. Schematic of the cathode is given in

Figure 1.12. Instead of tungsten emitter another type of alloy can also be used in this cathode. CPD with a tungsten surface has around 2 eV work function value and CPD with other alloy surfaces can have 1.8 to 1.9 eV work function values [28]. For more than thirty years, there are numerous research attempts and patents on controlling the porosity of cathodes, and consequently the barium diffusion and cathode emission [29].
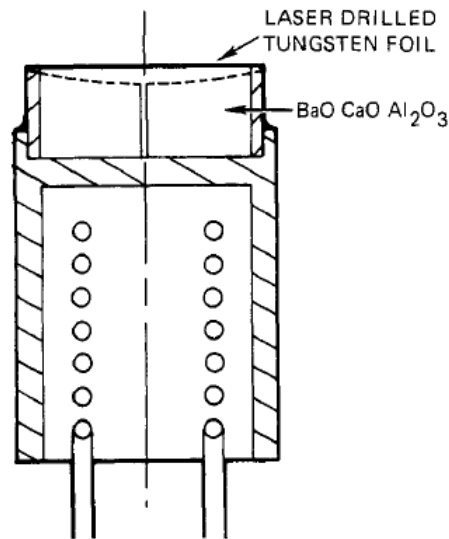
Figure 1.12. CPD cathode [28].

The difficulties of manufacturing and activation of L cathode forced researchers to develop more sophisticated cathodes. Impregnated dispenser cathodes eliminate the activation and manufacturing problems of L cathodes. It was found that, first of all making porous tungsten and then impregnating it with barium aluminate is more satisfying. The dispenser cathodes manufactured in this way have work function as high as 2.2 to 2.5 eV. Levi [30] discovered that the calcium addition to the impregnate mixture decreases the work function to the values around 2.1 eV. This dispenser cathode that contains calcium compounds within is called B type cathode.

The cathode widely used in thrusters is Phillips Type S cathode which has a porous tungsten matrix that is impregnated with an emissive mix of barium and calcium oxides and alumina. For instance, in an ion thruster mostly 4:1:1, where this notation represents the stoichiometric coefficient of $4BaO : 1CaO : 1Al_2O_3$, emmisive material is used. The 4:1:1 has a work function about 2.06 eV at temperatures around 800°C

[11, 31, 32]. Other commonly encountered impregnate compositions are 5:3:2 and 3:1:1. The most significant shortcoming of BaO emitters is that they are prone to poisoning due to impurities present in the propellant. Poisoning on the dispenser cathode can increase the work function and shorten the lifetime of the system. In the systems operating with BaO emitter, special care must be taken in order to prevent poisoning. Need of high purity propellant usage (about 99.999%) demands propellant purification system which causes a financial burden of 0.5-1 M$ per spacecraft [33].

The barium impregnated emitters require a special conditioning procedure prior to operation and in case of any exposure to atmosphere. After the system is evacuated to the pressures less than 1.3×10^{-4} Pa for at least 12 hours, the insert is heated to around 500 °C and kept at this temperature for three hours. Subsequently, the cathode heater is turned off for 30 minutes. Eventually, after heating the insert to a temperature around 1000 °C and keeping it at this temperature for one hour, it is allowed to cool down for 30 minutes. The purpose of this whole conditioning process is to eliminate the absorbed carbon dioxide and water in the insert material and make its surface ready for thermionic emission [34]. LaB_6 emitter, on the other hand, does not require any special conditioning procedure [27].

Another type of emitter is mixed metal matrix cathodes. According to the experiments, it is observed that the work function can be reduced if the tungsten matrix is introduced with refractory materials such as osmium, rhenium, iridium, dispenser cathode can have work function less than 1.9 eV. Mixed metal matrix cathodes are similar to conventional cathodes except for the usage of porous tungsten iridium (W-I) alloy as surface. In this type of matrix, less work function can be obtained which reduces the required temperature for a given emission current density [33].

Orifice is a refractory plate welded at the cathode tube exit. Orifice helps maintaining high internal pressures around $10^3 - 10^4$ Pa. The pressure inside the cathode must be high enough to create a collisional plasma. Hollow cathodes can be categorised under three classes in terms of the orifice geometry as shown in Figure 1.13. First type (Type A) has a small orifice with a large length to diameter ratio. This type of cathode
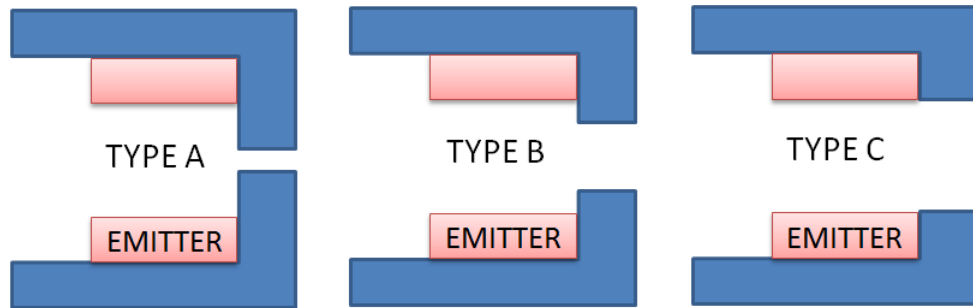
Figure 1.13. Different orifice constructions.

is operated at low current and high internal gas temperatures and heated by orifice heating. Second type of hollow cathode (Type B) has an orifice diameter larger than length and operate at lower gas pressures. Insert heating is provided with ion or electron bombardment, or depending on the orifice size and operating temperatures these two heating systems are used together. Third type of hollow cathode (Type C) has no orifice. In this design large neutral density gradient can be obtained however internal pressure is lower. The heating mechanism for third type cathodes is ion bombardment of the insert [11].

1.3. Overview of Hollow Cathode Physics

During the operation of a hollow cathode, there are two plasma regions, orifice and insert (emitter) plasma, in the interior of this device. The schematic of the plasma regions in an operating hollow cathode can be seen in Figure 1.14.

Creation of plasma in the hollow cathode requires ionization of the propellant gas. The electrons which ionize the propellant atoms are provided to the system from insert material by thermionic emission. At the initiation of the system, the insert is heated up to a temperature (typically between 1300 K and 1900 K) with an external heater wrapped around the refractory cathode tube. At this temperature the insert material starts to emit electrons. After electron emission begins, the propellant (generally xenon
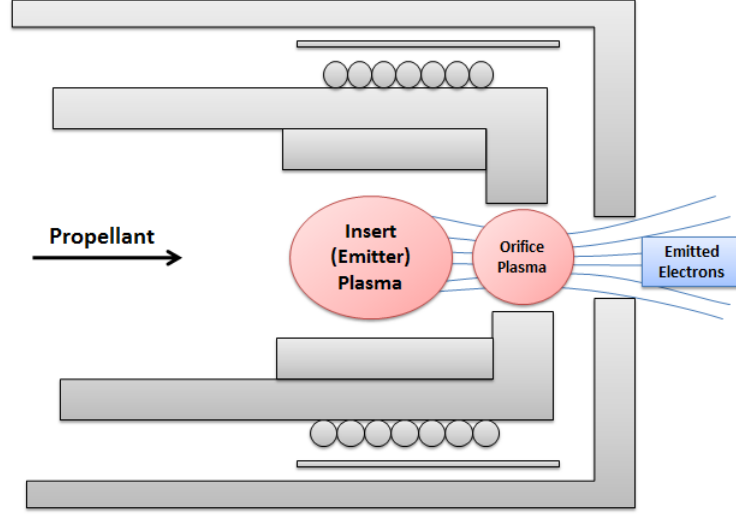
Figure 1.14. Schematic of hollow cathode in operation.

or argon) is injected to the cavity of the cathode tube. Once the propellant gas atoms reach the insert region, they collide with the emitted electrons and the insert plasma that is a combination of ions, electrons and neutral atoms is formed. The density of the insert plasma is generally on the order of 10^{20} m^{-3} and the temperature of the insert plasma is around 1-2 eV. The creation of a dense plasma in the insert region also prevents space-charge effects [35]. After creation of the plasma in the insert region, external heater is turned off and the amount of energy, which is needed to keep thermionic emission to continue, is sustained to the insert material by the ions and the electrons coming from insert region plasma and recombining on the cathode wall. Therefore, the system becomes self sustaining and it does not require any other energy sources. This self heating mechanism of insert in hollow cathodes depends on different parameters such as orifice diameter, propellant flow rate, discharge current. Once the plasma in the insert region is generated, discharge of electron begins due to the voltage difference originated from previously biased keeper.

When a material is heated up to a sufficient temperature, it starts to emit electrons. The density of the electron current emitted from material is given by well known Richardson-Laue-Dushman equation as follows:

$$J_{em} = AT_{w,ins}^2 e^{-\frac{q\phi_{wf}}{k_B T_{w,ins}}} \tag{1.1}$$

In Equation 1.2, Richardson constant, A, is equal to 120 $Acm^{-2}K^{-2}$, $T_{w,ins}$ is the surface temperature of the emitting material in K, ϕ_{wf} is a material dependent quantity known as work function in eV and k_B is Boltzmann's constant [11]. Derivation of Richardson-Laue-Dushman equation with thermodynamic approach can be found in Appendix B. Emission of electrons from insert material creates a negative potential on the insert surface. Thus, a sheath region develops on the insert material in order to balance electron and ion fluxes to the surface. Figure 1.15 shows the structure of this sheath. The sheath region present on the insert surface creates a retarding potential region for electrons. Hence, electrons coming from insert plasma must carry enough energy to overcome this retarding potential and reach the insert surface. The thickness of this sheath is on the order of several Debye lengths.
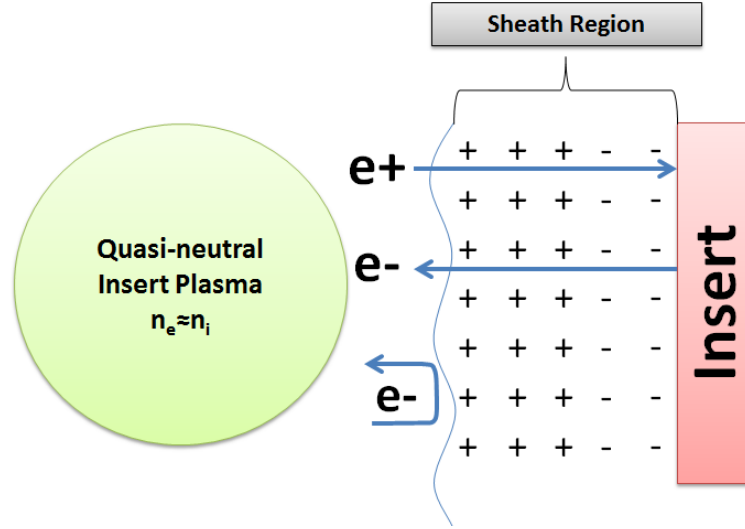
Figure 1.15. Schematic of sheath region developing on the insert material.

In the sheath region that develops on the insert material, a non-zero electric field, E_s, is created. This electric field acting on the emitter surface reduces the apparent work function of the material, and thus enhances the thermionic emission. The effective work function of the emitter material under an electric field can be calculated by the Schottky equation as follows:

$$\phi_{eff} = \phi_{wf} - \sqrt{\frac{qE_s}{4\pi\epsilon_0}} \tag{1.2}$$

In the orifice region, more collisional and denser plasma is created during operation. The highest current density appears in the orifice among all system sections. Double sheath, formed between the insert region and orifice region, accelerates the insert electrons into the orifice and orifice ions into the insert region. The sheath region develops on the orifice surface as given in Figure 1.16 [34].
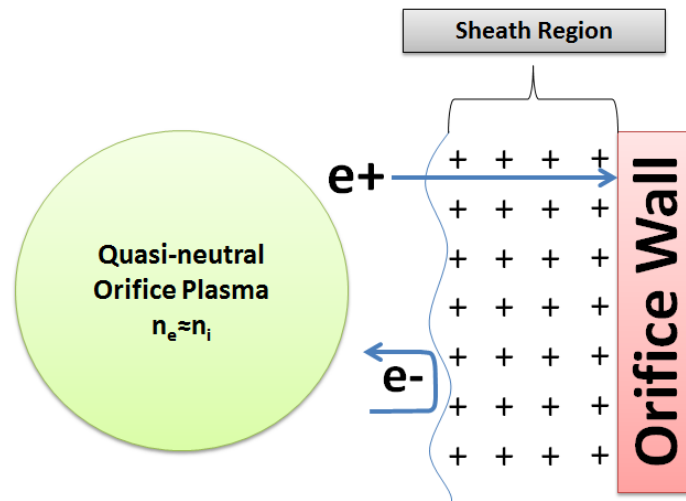
Figure 1.16. Schematic of the sheath developing on the orifice wall.

The Debye length is much smaller compared to the orifice diameter. Mean free paths of most collisions in the orifice are ten to one hundred times smaller compared to the orifice dimensions and thus majority of ions generated in the orifice recombine on the orifice wall. The generation of ions with both electron impact ionization and stepwise ionization mechanisms are sufficient to counterbalance the loss of ions [36]. Density of the orifice plasma is generally on the order of 10^{21} m^{-3} and the plasma temperature is around 2 eV. Design of orifice can play a significant role on the performance and the operation parameters of hollow cathode. Pressure of neutral particles in the insert region plasma is an important parameter which affects the plasma density. The size of the orifice is a factor that determines the cathode internal pressure. Furthermore, propellant and power consumption of a hollow cathode operating at spot mode is strongly tied to the orifice dimensions. Smaller orifice could decrease the penetration of the potential, applied from keeper, to internal region and as a result, discharge initiation can be difficult.
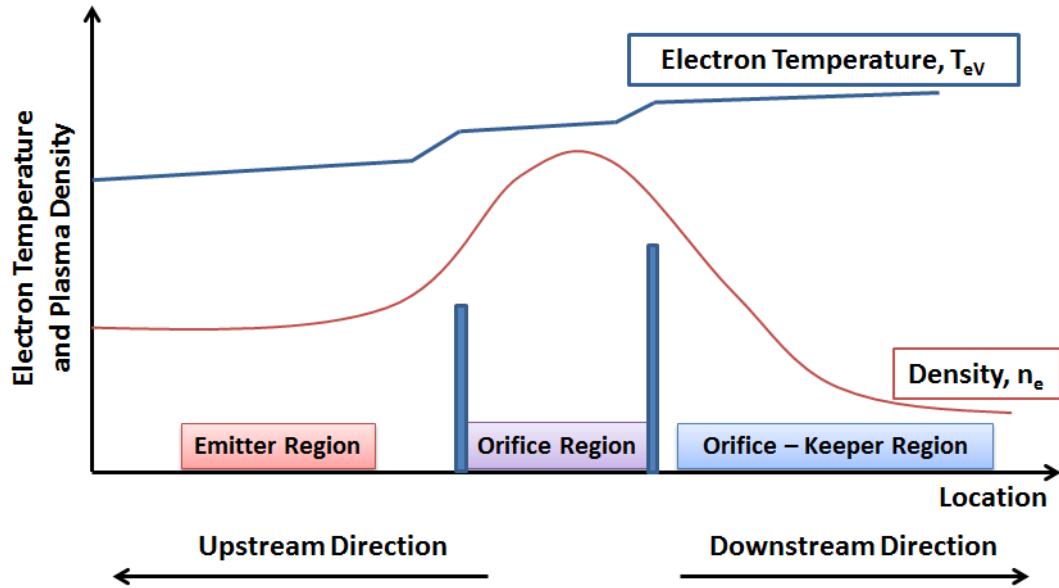
Figure 1.17. Axial plasma density and plasma temperature profile along hollow cathode regions [37, 38, 39].

Explaining briefly the plasma conditions in the hollow cathode would also be beneficial in order to understand the hollow cathode operation. The axial electron temperature and density of the plasmas in the distinct regions of hollow cathode are given in Figure 1.17. The axial density of the insert plasma increases in the region close to the orifice entrance. A peak in the plasma density is seen in the orifice region. In the gap between orifice and keeper, a sharp decrease in the plasma electron density occurs. The plasma temperature in the insert region is around 1 eV. Due to the presence of more collisional and denser plasma in the orifice region, the plasma electron temperature increases. In the interior region of an OHC, the electron temperature increases due to classical collisions. However, in the vicinity of the orifice, the electrons are heated up due to electrostatic instabilities [39].

1.4. Plume and Spot Mode Operation of Hollow Cathodes

Operation of hollow cathodes at spot and plume modes is important for performance characterization of these devices. At spot mode operation the voltage is weakly dependent on the flow rate. Another characterization of spot mode is also defined as

observing small, luminous region at the orifice exit and having negligible AC components in discharge voltage. At spot mode operation, the plasma present in the gap between orifice to keeper has sufficient density so that the required amount of current can be collected passively at the keeper or anode. At spot mode operation, negligible voltage fluctuation is observed. This operation mode can be achieved at high current and high flow rates. At this operation mode, a quasi-neutral plasma is present, accompanying a small sheath region developed around keeper orifice, between the orifice and the keeper [34, 40].

At low currents and flow rates, the collection of electrons at keeper is not sufficient. Therefore, sheath thickness increases in order to attract the electrons towards the keeper or the anode. This mode of operation is called plume mode. At plume mode operation, a luminous region occurs in front of the orifice region and beyond the keeper orifice [9, 36]. Another characteristic of plume mode operation is high discharge voltages and large fluctuations in voltage which is necessary to obtain desired current. Furthermore, electron temperatures increase at plume mode operation because of the reduced inelastic collisions and the low density [41]. Due to high voltage demand at plume mode operation, the power consumption of cathode increases. Another shortcoming of operation at plume mode is that ions repelled by keeper cause sputtering on orifice of the cathode [42]. Therefore, plume mode operation reduces the lifetime of hollow cathode.

1.5. Literature Review

Since hollow cathodes have been under investigation, numerous studies have been published in order to assess the plasma parameters in these devices. In the study published by Katz *et al.* [43], sensitivity of hollow cathode, operating in spot mode, to orifice diameter, orifice length, propellant mass flow rate and keeper current was investigated. In this parametric study, ion temperature and neutral temperature are assumed to be 0.1 eV. The plasma energy gain due to ohmic heating is equated with ionization loss, excitation loss and electron convection loss. The orifice plasma temperature and plasma density were varied until ion loss balances ion gain, and energy loss

equals to energy gain. Different parameters such as orifice length, discharge current are doubled to see the influence on hollow cathode and some of the results are given in Table 1.1.

Table 1.1. Calculated results for varying model parameters [43].

Diameter [mm]	Length [mm]	Discharge [A]	Mass Flow Rate [sccm]	I^2R [W]	Energy For Each Ion Generation [eV/ion]
1	6	1	2	22.31	3.952
1	12	1	2	44.26	7.315
0.7	6	1	2	40.44	5.312
1	6	1	4	25.10	4.270
1	6	2	2	35.06	2.879

Another modelling attempt of orificed hollow cathode was published in 2012 by researchers from Israel Institute of Technology [44]. A zero dimensional (0-D) model for orifice plasma was developed for large aspect ratio cathodes (L/2r). In this model, some plasma parameters are considered as nonuniform. The electron temperature, neutral gas temperature, electron current, axial neutral gas velocity (T_e, T_0, I_e, u_0) are taken as constant in the orifice. Neutral density and neutral gas velocity vary only in axial direction. The plasma density in the orifice changes in both axial and radial directions, $n(r, z)$. The equations of motion for ions and neutrals are defined in terms of averaged parameters in order to come up with a set of algebraic equations. Even tough it is a zero dimensional model, the plasma parameters show good agreement with two dimensional (2-D) models. Moreover, its computational time is much shorter than one dimensional (1-D) or 2-D models.

Most recent study on 0-D modelling of hollow cathode is published in 2013 by Italian researchers in Alta group [45]. The most prominent feature of this model is that it does not require any kind of external input such as experimental data. This model consists of three main parts; orifice model, emitter model and thermal model. The plasma density, electron temperature, neutral density in the orifice and emitter regions are obtained after orifice and emitter iterations. The thermal model is used to obtain temperature along the cathode. The cathode is considered as if it is composed

of several sub elements which are in contact with each other with perfect gluing and the thermal network between these sub elements are developed. The ion conservation, plasma energy balance and pressure balance equations are solved in the orifice region. Even tough the continuum assumption is not valid in orifice region ($0.01 < Kn < 0.05$), the pressure equation equates the pressure of a continuum flow with the one calculated from kinetic theory of gases. Similarly, in addition to ion conservation, plasma energy balance and pressure balance equations, current density equation is also solved in the emitter model. The nonlinear equation sets that occur as a result of governing equations in the emitter and orifice regions are solved by using Matlab fsolve command. Despite the fact that this model cannot answer the significant changes in geometry, mass flow rate and discharge current, it is the most comprehensive 0-D model of hollow cathode. The effect of the viscosity is not taken into account in this study. This is another shortcoming of this model since it can increase the inner pressure and neutral density by 50% [46].

In addition to zero dimensional models, there is also a one dimensional hollow cathode model in the literature. In the study published by Katz *et al.* in 2003 [37], a one dimensional hollow cathode model is developed based on the observation that ion mobility is diffusion limited. The continuity equations written for electrons, ions and neutrals, ion and electron momentum equations, energy equation for electrons are solved for modelling the hollow cathode plasmas. In this model, chamfered region next to the orifice is also taken into account. It is assumed that electrons behave as fluid. Orifice plasma loses xenon atoms and electrons from downstream, and xenon ions both from downstream and upstream. For insert region, isothermal ambipolar diffusion equation in two dimensions is solved to obtain the spatial distribution of insert plasma density.

Apart from zero dimensional and one dimensional modelling, there are also two dimensional modelling studies in the literature. Mikellides *et al.* developed a two dimensional axisymmetric model (Orifice Cathode OrCa2D) for OHCs with two different geometries [35, 38]. The modelled cathode diameters are 0.635 cm and 1.5 cm with a length of 2.54 cm, orifice diameter of 0.1 cm and 0.3 cm. The plasma is considered

as fluid, and governing equation are solved in a 2D computational domain in order to obtain two dimensional distribution of plasma density, electron current density, plasma temperature, electric field, plasma potential, neutral density and temperature of heavy particles. At the orifice entrance, plasma density and potential are set according to the experimental values and adiabatic condition is applied for electron temperature. At the cathode inlet, heavy species are considered at the wall temperature, adiabatic condition is applied for electrons and no electron flux is allowed. At orifice wall, zero electron emission is considered and temperature of the heavy particles is assumed to be equal to the wall temperature. After implementation of boundary condition and solution of governing equations with finite volume method, it is found that the neutral gas heating mechanisms is dominated by resonant charge-exchange collisions between fast ions and slow neutrals in case of inviscid flow.

As an extention of the OrCa2D model, several studies have been also published to assess different aspects. For instance, in the study published by Mikellides [47], the main goal was to asses the effect of viscosity. The governing equations are solved by finite volume approach for species present in the plasma after addition of viscous term in neutral momentum equation. The results, obtained by comparing the viscous and inviscid solutions, showed that viscosity has a significant influence on the flow field of the atomic species. Cathode internal pressure is found to be more than 40% higher than the inviscid solution. As a result, the force due to pressure gradient is larger than the drag force due to ion-atom collisions and reverses the flow field towards the cathode orifice region. On the other hand, it is found that the ions remain unaffected by viscous effect because motion of these species are mostly driven by electric field in the plasma and sheath regions instead of collisional drag forces. In another study published by Mikellides *et al.* [39], it was shown by the experimental measurements and numerical simulations, conducted on a 1.5 cm diameter hollow cathode operating at 25-27.5 A discharge current and 5.5 sccm xenon flow rate, that in the vicinity of the orifice, the electrons are heated up by electrostatic instabilities. Therefore, heating of electrons cannot be accounted by classical transport and Ohm's law. In this manner, there are several studies published in extension of OrCa2D by Mikellides *et al.* [46, 48, 49] and by Katz *et al.* [50].

Boyd & Crofton [51] developed a hybrid Particle in Cell (PIC) model for the plasma plume of an orificed hollow cathode. The hollow cathode modelled in this study has an impregnated tungsten dispenser whose inner diameter is 1 mm, outer diameter is 2.8 mm and length is 11 mm. The orifice diameter is 0.2 mm and length is 1 mm. The downstream of the orifice has a full-angle 90° chamfer. In this study, electrons are modelled by fluid equations, while heavy particles (ions and neutrals) are modelled kinetically using PIC method. Plasma density and plasma electron temperature at the HC exit are used as boundary conditions in PIC model.

Levko *et al.* [52] developed a two dimensional PIC simulation with Monte Carlo collison model for orificed micro hollow cathode. Effect of different values of Xe gas pressure, orifice size and operation voltage are assessed with the developed model. In this model, the electron-ion recombination, secondary electron emission due to bombardment by plasma ions and collisions between electron and neutral particles, thermionic electron emission corrected with the Schottky effect are included. The micro hollow cathode simulated with this code operated in a planar diode and at gas pressures greater than 50 Torr. The geometry of the orificed micro hollow cathode modelled in this study can be seen in Figure 1.18.
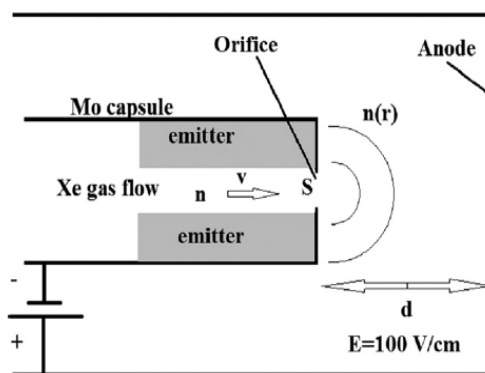
Figure 1.18. The geometry modelled in reference [52].

2. GLOBAL NUMERICAL MODEL FOR ORIFICED HOLLOW CATHODE

As mentioned before, modelling of the hollow cathode is important in order to understand the behaviour of this device and also results of the models can give vital information for building better systems. The theoretical modelling can give valuable clues about the effect of the geometry and operating conditions on the cathode behaviour, power consumption and lifetime. Mainly, the goal of the modelling attempts is to obtain main plasma parameters such as electron, neutral, ion density and temperature in the insert and orifice regions.

Since operation conditions and geometry are important for cathode performance [42], the primary aim of the developed model is to assess the cathode for different geometry and operating conditions. A quasi-neutral plasma with uniform plasma parameters (electron density, electron temperature, neutral density etc.) in both emitter and orifice region is assumed in this model. Orifice and emitter plasmas consist of a combination of thermalized electrons, singly-charged ions and neutrals, and they are enclosed within a hypothetical cylindrical control volume. The model considers that the particles in both plasma regions have Maxwellian distribution. In the model, it is assumed that the heavy particles, namely neutrals and ions, have the same temperature with the cathode wall. The developed model follows the previous studies of different researchers [11, 34, 45].

2.1. Insert Model

Considering steady state operation, ion balance, insert plasma power balance and current balance equations are solved in the hypothetical control volume enclosing the insert plasma as schematically shown in Figure 2.1. Eventual goal of the insert plasma model is to compute the plasma number density, plasma electron temperature, emitter wall temperature, and the influence of the operation conditions and geometry on insert

plasma parameters and emitter wall temperature.
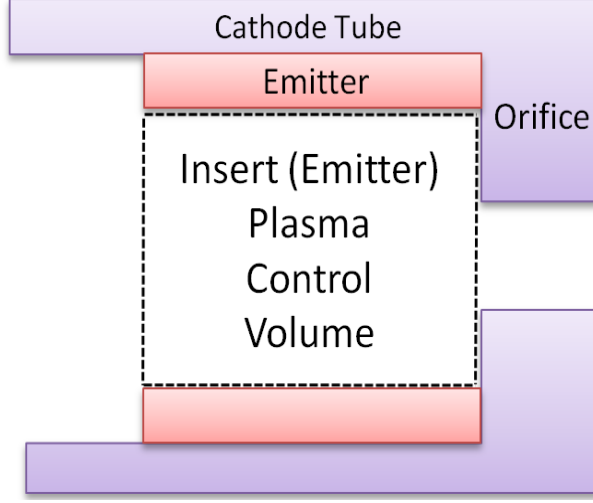
Figure 2.1. Insert plasma control volume.

2.1.1. Ion Conservation

There are two types of electron populations that can cause ionization events in the insert region: low-temperature electrons emitted from the insert material with thermionic emission and the Maxwellian plasma electrons present in the insert plasma. The energy spent for ionization and excitation events due to the Maxwellian electrons can be evaluated as follows:

$$\left(\frac{dn_i}{dt}\right)_{ionization} qU_i = q\pi r_e^2 L_{emit} U_i N_e n_e \langle \sigma v_e \rangle \qquad [W] \qquad (2.1)$$

$$\left(\frac{dn_{exc}}{dt}\right)_{excitation} qU_{exc} = q\pi r_e^2 L_{emit} U_i N_e n_e \langle \sigma^* v_e \rangle \qquad [W] \qquad (2.2)$$

According to [34], the electron-impact ionization due to the electrons emitted from insert material is negligible. Therefore, ionization mechanisms in the insert plasma are electron-impact and stepwise ionization due to Maxwellian electrons in the insert plasma, and stepwise ionization due to primary electrons (electrons emitted from insert material).

The ionization term in the ion conservation equation considers only the electron-impact ionization from the ground state, and stepwise ionization processes are neglected. As shown in Figure 2.2, the ion loss mechanism in this region is the thermal flux of ions towards the cathode base and the strike of ions to the surface of the insert material and orifice wall. The ion generation mechanism, on the other hand, is ion production due to the electron impact ionization. The ion conservation in steady-state operation is given as:

$$\underbrace{q\pi r_e^2 L_{emit} N_e n_e \langle \sigma v_e \rangle}_{\substack{\text{Ion generation with} \\ \text{electron impact ionization}}} = \underbrace{J_{i,Th}\left(\pi r_e^2\right)}_{\substack{\text{Thermal ion loss} \\ \text{to upstream}}} + \underbrace{J_{i,Bohm}\left(2\pi r_e L_{emit} + \pi r_e^2\right)}_{\substack{\text{Ion loss to insert surface} \\ \text{and to orifice region}}} \tag{2.3}$$

The left hand-side of Equation 2.3 represents the amount of ion produced by electron impact ionization from the ground state. Here, n_e and N_e represents plasma density and neutral density of emitter region plasma, respectively. The first term on the right hand side stands for the thermally lost ions to upstream and the second term on the right hand side shows the ion loss to the insert surface and orifice wall. Even tough, it is speculated by [53] and experimentally observed by [54] that a double layer is formed at the constriction between insert and orifice region plasma, effect of this double layer structure is not taken into account in Equation 2.3. As found in studies [44] and [46] for xenon flow rate higher than 1 sccm, neutral gas flow sweeps the ions from insert to orifice. Thus, this is also accounted in the ion conservation Equation 2.3. Therefore, this model is expected to be more accurate for flow rates greater than 1 sccm.
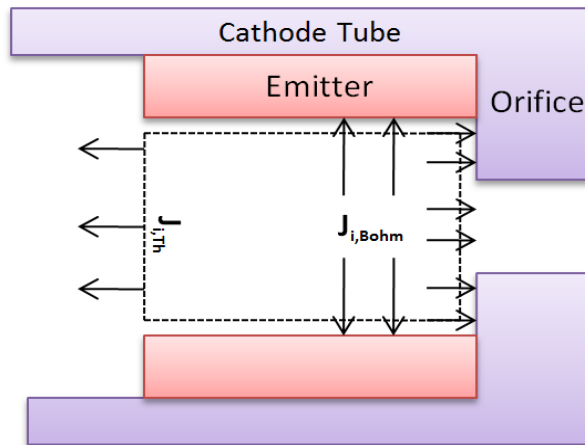
Figure 2.2. Mobility of ions in the emitter region.

The ionization rate function, as a function of electron temperature, T_{eV}, is calculated according to the expression given in [11] as follows:

$$\langle \sigma v_e \rangle = 10^{-20} \left[\left(3.97 + 0.643 T_{eV} - 0.0368 T_{eV}^2 \right) e^{\frac{-12.127}{T_{eV}}} \right] \left(\frac{8 q T_{eV}}{\pi m_e} \right)^{1/2} \qquad \left[\frac{m^3}{s} \right] \quad (2.4)$$

2.1.2. Insert Plasma Energy Balance

Apart from ion conservation, energy balance equation of the emitter plasma is also solved. The energy balance for the insert region plasma involves all the energy that comes in and out of the plasma region. In the insert region of the hollow cathode, the energy gain of the plasma due to ohmic heating and thermionic electron emission is balanced by the energy loss due to ions leaving the control volume, random electron current to the insert surface and electron discharge current. In energy balance equation, it is considered that the plasma is optically thick, so that radiated energy is again absorbed by the plasma. Thus, radiation losses are not considered [55]. Energy removed via excitation is also ignored in the energy balance equation written for insert region plasma [11]:

$$\underbrace{I_{em} \phi_s}_{\substack{\text{Gain due to} \\ \text{thermionic electron emission}}} + \underbrace{R_e I_d^2}_{\substack{\text{Gain due to} \\ \text{ohmic heating}}} = \underbrace{I_{i,out} \left(U_i + \frac{2 k_B T_{w,ins}}{q} \right)}_{\substack{\text{Loss due to} \\ \text{ion loss}}}$$
$$+ \underbrace{\left(2 T_{eV,ins} + \phi_s \right) I_r}_{\substack{\text{Loss due to} \\ \text{random electron current}}} + \underbrace{\frac{5}{2} T_{eV,ins} I_d}_{\substack{\text{Loss due to} \\ \text{electron discharge}}} \qquad (2.5)$$

Here I_{em} represents the thermionic emission current in Amperes, ϕ_s represents the sheath voltage built in plasma in Volts, R_e is the resistance of the plasma in Ohms, I_d is the current extracted from the cathode in Amperes, $I_{i,out}$ is the ion current out of the control volume in Amperes, U_i is the first ionization energy of xenon in eV, T_{eV} is electron temperature in eV, and I_r is the random electron current to the insert surface in Amperes at the insert region [11].

$I_{em}\phi_s$ term represents the energy input by thermionically emitted electrons that are accelerated by sheath plasma potential. $R_eI_d^2$ term represents the energy lost by the electrons to the plasma due to collisions with the ions and the neutrals in the plasma. First term on the right hand side accounts for the energy lost due to the ions leaving the control volume. $(2T_{eV,ins}+\phi_s)I_r$ term represents the energy that is drawn from the plasma as the electrons overcome the sheath potential at the sheath edge and reaches the insert wall. $\frac{5}{2}T_{eV,ins}I_d$ term is the energy spent to energize the extracted current. Here 3/2 of this represents total kinetic energy in three degrees of freedom (x, y, z, 1/2 each) and 1 comes from work done on the electrons by pressure. As the current is extracted, this energy is carried away.

In order to calculate emitter plasma energy gain due to ohmic heating, the emitter plasma resistance, R_e, is found from the following expression [34]:

$$R_e = \eta\frac{r_e}{4/3r_eL_{emit}} \qquad [ohm] \qquad (2.6)$$

where L_{emit} is the length of the actively emitting region of the emitter, also corresponding conduction length of the plasma, r_e is the radius of the emitter region plasma, η is the resistivity of the insert region plasma. It is assumed that most of the current is carried in radial direction, thus for the current conduction an average cross-sectional area is used as given in [34]. The resistivity of the plasma is given by:

$$\eta = m_e\frac{\nu_{ei}+\nu_{en}}{q^2n_e} \qquad \left[\frac{kg \times m^3}{s \times C^2}\right] \qquad (2.7)$$

where n_e is emitter plasma density, q is the electron charge, ν_{ei} and ν_{en} are electron-ion and and electron-neutral collision frequencies respectively. The electron-ion collision frequency is calculated as follows:

$$\nu_{ei} = 2.9 \times 10^{-12}\frac{n_e\Lambda}{T_{eV,ins}^{3/2}} \qquad \left[\frac{1}{s}\right] \qquad (2.8)$$

where the quantity Λ, is the Coulomb logarithm and it is given as:

$$\Lambda = 23 - \frac{1}{2} \ln \left(\frac{10^{-6} n_e}{T_{eV,ins}^3} \right) \tag{2.9}$$

The electron-neutral collision frequency is given by:

$$\nu_{en} = \sigma_{en} N_e \sqrt{\frac{8 k_B T_{e,ins}}{\pi m_e}} \qquad \left[\frac{1}{s} \right] \tag{2.10}$$

where σ_{en} is the electron-neutral collision cross section:

$$\sigma_{en} = 6.6 \times 10^{-19} \left[\frac{\frac{T_{eV,ins}}{4} - 0.1}{1 + \left(\frac{T_{eV,ins}}{4} \right)^{1.6}} \right] \qquad [m^2] \tag{2.11}$$

2.1.3. Current Balance

Another equation written for the emitter plasma region is the current balance. There are four currents that play part in the plasma as shown in Figure 2.3. In this figure the dashed line represents the sheath edge of the plasma at the insert region.
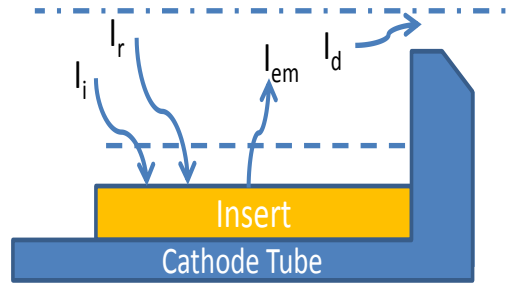
Figure 2.3. Schematic of the current balance in the insert region.

The four currents that enter and leave the insert region plasma have the following relationship [11]:

$$\underbrace{I_{em}}_{\substack{\text{Thermionically emitted} \\ \text{electron current}}} + \underbrace{I_i}_{\substack{\text{Ion current to the} \\ \text{insert surface}}} = \underbrace{I_d}_{\text{Discharge current}} + \underbrace{I_r}_{\substack{\text{Random electron current} \\ \text{to the insert surface}}} \tag{2.12}$$

In this equation, I_{em} is the amount of electron current emitted from insert with thermionic emission. Thus, I_{em} represents the total electron current leaving the insert surface and entering the insert region plasma. The thermionic current density is evaluated from Richardson-Laue-Dushman equation:

$$J_{em} = DT_{w,ins}^2 exp\left(-\frac{q\phi_{eff}}{k_B T_{w,ins}}\right) \qquad \left[\frac{A}{m^2}\right] \tag{2.13}$$

where D is material constant and $T_{w,ins}$ is the emitter wall temperature. D is taken as 29 $Acm^{-2}K^{-2}$ for LaB_6 [16].

In the presence of an electric field on the insert material, the apparent work function decreases. This phenomena is referred to as the Schottky effect and effective work function is given as:

$$\phi_{eff} = \phi_{wf} - \sqrt{\frac{qE_s}{4\pi\epsilon_0}} \qquad [V] \tag{2.14}$$

where ϕ_{wf} is the value of the work function in the literature, E_s is the electric field of the cathode sheath acting on the insert material and it is given as follows [56]:

$$E_s = \sqrt{\frac{n_e k_B T_{e,ins}}{\epsilon_0}} \left[2\sqrt{1 + \frac{2q\phi_s}{k_B T_{e,ins}}} - 4\right]^{1/2} \qquad \left[\frac{V}{m}\right] \tag{2.15}$$

where ϕ_s, the emitter sheath voltage drop, is given as [11]:

$$\phi_s = \frac{k_B T_{e,ins}}{q} ln\left[\sqrt{\frac{2m_i}{\pi m_e}}\right] \qquad [V] \tag{2.16}$$

The electric field caused by the sheath potential on the emitter reduces the literature work function of insert material, and thus enhances the thermionic electron emission. Eventually, electron emission current from insert with field-enhanced thermionic emission can be calculated as follows:

$$I_{em} = J_{em} A_{emit} \qquad [A] \tag{2.17}$$

I_i is the ion current that leaves the insert region plasma and reaches the surface of the emitter. These ions that reach the surface bombard the surface with their energy and contribute to the heating of the surface. I_i is calculated from Bohm sheath criterion as follows:

$$I_i = 0.61 q n_e \sqrt{\frac{k_B T_{e,ins}}{m_i}} A_{emit} \qquad [A] \qquad (2.18)$$

where n_e is the electron density in the insert region plasma, $T_{e,ins}$ is electron temperature in K. In Equation 2.12, I_r, the random electron current at the sheath edge, is given by:

$$I_r = \frac{1}{4} n_e q \left(\frac{8 k_B T_{e,ins}}{\pi m_e} \right)^{1/2} \exp \left(\frac{-q \phi_s}{k_B T_{e,ins}} \right) A_{emit} \qquad [A] \qquad (2.19)$$

The neutral density in the insert region is determined by assuming Pouiselle flow through the orifice. Taking reduced temperature T_r as the ratio $T_n/289.7$. The viscosity is given by [11]:

$$\zeta = 2.3 \times 10^{-4} T_r^{0.71 + \frac{0.29}{T_r}} \qquad [Poise] \qquad (2.20)$$

Then the pressure of neutral atoms will be determined in terms of Torr as follows [11]:

$$P = \sqrt{\frac{0.78 Q \zeta T_r L_o}{d_o^4}} \qquad [Torr] \qquad (2.21)$$

where L_o and d_o are orifice length and diameter in cm respectively, Q is the mass flow rate in sccm. Finally, neutral density in the insert plasma, N_e, is found from:

$$N_e = 9.65 \times 10^{24} \frac{P}{T_n} \qquad [m^{-3}] \qquad (2.22)$$

During the operation of hollow cathode, density of the insert plasma becomes greater in the region close to the orifice. Especially, operation at high currents and mass flow rates pushes the plasma density peak to the regions closer to orifice [37, 38, 57]. There-

fore, this peak in insert plasma density causes small plasma-emitter contact area. As a result of this small plasma-emitter attachment area, required current is emitted from that small region close to orifice which leads high current density and high temperature as speculated in studies [11, 37, 50]. In other words, this uneven distribution of temperature on the emitter surface causes the hotter regions to emit more electrons. For determination of the effective emission length of the insert, the simple methodology proposed by Alta group is used. It is assumed that the product of the effective emission length and the insert plasma pressure is equal to 15 mPa. It is suggested that even tough the product of the effective emission length and the insert plasma pressure is set equal to 5 mPa or 10 mPa, it does not affect the general tendency of the plasma parameters [45].

$$15 = L_{emit} \times P \times 133.322 \qquad [mPa] \qquad (2.23)$$

where P is in terms of Torr.

2.2. Orifice Model

Electrons coming from the insert region experience frequent elastic and inelastic collisions in the orifice region. These collisions create resistance to the electron current. Throughout orifice modelling, thermionic emission from the orifice material is ignored because common materials used as orifice have high work function (i.e. 4.5 eV for tungsten). This orifice model follows the work done by [11, 43]. Considering steady state operation, ion balance in radial direction, plasma power balance and energy balance written for orifice surface equations are solved in the hypothetical control volume enclosing orifice plasma as schematically shown in Figure 2.4. Eventual goal of the orifice plasma numerical model is to compute the plasma number density, plasma electron temperature, orifice wall temperature and the influence of the operation conditions and geometry on orifice plasma parameters.
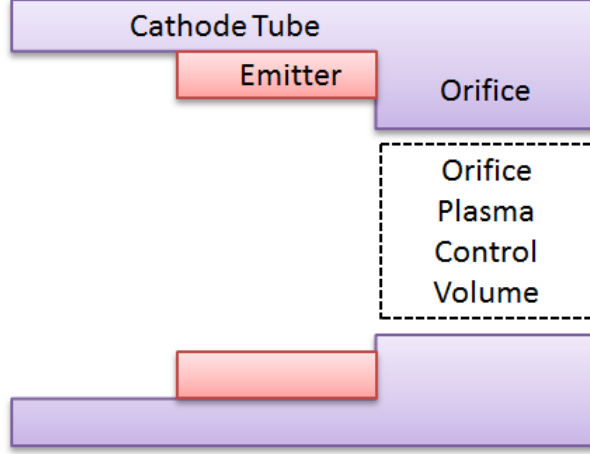
Figure 2.4. Orifice plasma control volume.

2.2.1. Ion Conservation

The temperature of the orifice plasma is calculated with mathematical expression that is given under the assumption of large aspect ratio ($L_o/(2r_o) > 1$) in [11]. The electron temperature, $T_{eV,orf}$, in a long plasma is identified by balancing radial ion loss due to diffusion with ion generation since majority of ions generated in the orifice recombine on the orifice wall [36]. A radial diffusion equation can be written by balancing radial ion loss due to diffusion with ion generation as follows:

$$-\nabla \cdot [D_a \nabla n] = \dot{n} \tag{2.24}$$

In Equation 2.24, D_a represents the ambipolar diffusion coefficient. The solution of this ion radial diffusion equation, whose solution procedure is elaborated in Appendix C, gives rise to eigenvalue equation which only has dependence on the electron temperature [11, 12]

$$\left(\frac{r_o}{\lambda_{01}}\right)^2 N_o \sigma_i \left(T_{e,orf}\right) \sqrt{\frac{8k_B T_{e,orf}}{\pi m_e}} = \frac{q}{m_i} \frac{T_{iV,orf} + T_{eV,orf}}{\sigma_{cex} N_o} \sqrt{\frac{m_i}{k_B T_{i,orf}}} \tag{2.25}$$

where λ_{01} is the first zero of the zeroth order Bessel function of the first kind, N_o is orifice neutral number density, σ_{cex} is resonant charge exchange cross-section and has the value of 10^{-18} m^2 [11], σ_i is ionization cross section averaged over Maxwellian electron

temperature and $T_{i,orf}$ and $T_{iV,orf}$ are ion temperature in K and eV, respectively.

2.2.2. Orifice Plasma Energy Balance

Orifice plasma energy balance equates the energy gain of the plasma due to resistive heating with the energy loss due to ionization and convection of electrons from orifice to insert. Since the electron temperature in the orifice is larger in comparison to the insert plasma electron temperature, the convection loss occurs. The energy equation for orifice plasma is written as follows:

$$\underbrace{R_o I_d^2}_{\substack{\text{Energy gain due to} \\ \text{ohmic heating}}} + \underbrace{2.5 \frac{k_B}{q} I_d T_{e,ins}}_{\substack{\text{Energy gain due to} \\ \text{electrons coming from insert}}} = \underbrace{q \pi r_o^2 L_o N_o n_o \langle \sigma v_e \rangle U_i}_{\text{Energy loss due to ionization}}$$

$$+ \underbrace{2.5 \frac{k_B}{q} I_d T_{e,orf}}_{\substack{\text{Energy loss due} \\ \text{electrons leaving orifice}}} \tag{2.26}$$

When we put Equation 2.26 in a tidy form, we end up with the following expression:

$$\underbrace{R_o I_d^2}_{\substack{\text{Energy gain due to} \\ \text{ohmic heating}}} = \underbrace{\left(q \pi r_o^2 L_o N_o n_o \langle \sigma v_e \rangle \right) (U_i)}_{\text{Energy loss due to ionization}} + \underbrace{2.5 \frac{k_B}{q} I_d \left(T_{e,orf} - T_{e,ins} \right)}_{\substack{\text{Energy loss due} \\ \text{electron convection}}} \tag{2.27}$$

In Equation 2.27, the term on the left is the energy gain due to ohmic heating, the first term on the right is energy loss due to ionization and finally the last term is the energy loss due to electron convection. Orifice plasma resistance is evaluated as follows

$$R_o = \frac{\eta L_o}{\pi r_o^2} \qquad \left[\Omega = \frac{m^2 \times kg}{s \times C^2} \right] \tag{2.28}$$

where the resistivity term, η, is:

$$\eta = \frac{\nu m_e}{n_o q^2} \qquad \left[\frac{kg \times m^3}{s \times C^2} \right] \tag{2.29}$$

where ν stands for total collision frequency. In total collision frequency calculation, the contribution of both electron-ion and electron-neutral collisions are taken into account as follow:

$$\nu = \nu_{ei} + \nu_{en} \qquad \left[\frac{1}{s}\right] \tag{2.30}$$

where electron-ion collision frequency, ν_{ei}, is:

$$\nu_{ei} = (2.9 \times 10^{-12})\frac{n_o\Lambda}{(T_{eV})^{3/2}} \qquad \left[\frac{1}{s}\right] \tag{2.31}$$

where the quantity Λ, is the Coulomb logarithm and it is:

$$\Lambda = 23 - \frac{1}{2}\ln\left(\frac{10^{-6}n_o}{T_{eV}^3}\right) \tag{2.32}$$

Electron-neutral collision frequency is given by:

$$\nu_{en} = \sigma_{en}N_o\sqrt{\frac{kT_e}{m_e}} \qquad \left[\frac{1}{s}\right] \tag{2.33}$$

where σ_{en} is electron-neutral collision cross section and it is given as:

$$\sigma_{en} = 6.6 \times 10^{-19}\left[\frac{\frac{T_{eV}}{4} - 0.1}{1 + \left(\frac{T_{eV}}{4}\right)^{1.6}}\right] \qquad [m^2] \tag{2.34}$$

where T_{eV} is the electron temperature in terms of eV.

Finally, the amount of power transferred to orifice plasma with ohmic heating can be calculated as:

$$P_R = R_o I_d^2 \qquad [W] \tag{2.35}$$

The power loss due to neutral particle ionization in the orifice is:

$$P_{ion} = \left(\frac{dn_i}{dt}\right)_{ionization} qU_i = q\pi r_o^2 L_o U_i N_o n_o \langle \sigma v_e \rangle \qquad [W] \qquad (2.36)$$

where n_o can be evaluated from the solution of Equation 2.25, and U_i, which is the mean energy loss due to single ionization event, is 12.1 eV for Xenon. In order to calculate the neutral particle number density in orifice plasma, it is assumed that choked flow condition occurs at the orifice exit. Under this assumption orifice plasma neutral number density can be calculated as follows [58]:

$$N_o = \frac{\dot{m}}{M_o A_{orf} \sqrt{\gamma R_g T_{w,orf}}} \qquad [m^{-3}] \qquad (2.37)$$

For calculation of the ionization rate function, the expression, which is a function of plasma electron temperature, given in [11] is used:

$$\langle \sigma v_e \rangle = 10^{-20} \left[\left(3.97 + 0.643 T_{eV} - 0.0368 T_{eV}^2 \right) e^{\frac{-12.127}{T_{eV}}} \right] \left(\frac{8q T_{eV}}{\pi m_e} \right)^{1/2} \qquad \left[\frac{m^3}{s} \right] \quad (2.38)$$

Loss due to electron convection is given as:

$$P_{conv} = 2.5 \frac{k_B I_d}{q} (T_{e,orf} - T_{e,ins}) \qquad [W] \qquad (2.39)$$

2.2.3. Orifice Wall Energy Balance

Another equation written for the orifice model is the energy balance on the orifice surface. The ions passing the sheath reaches the orifice and give their energy to the orifice. Electrons striking the orifice surface are also another energy gain mechanism. The energy loss mechanisms for the orifice is the heat conduction to the base and the insert, and thermal radiation to its surroundings. Figure 2.5 depicts the energy exchange in the orifice. Under these conditions, orifice wall energy balance can be

written as follows:

$$\underbrace{I_{Bohm,orf}\left(U_i + \phi_{s,orif} + 0.5\frac{k_B T_{w,orf}}{q}\right)}_{\text{Ion heating}} + \underbrace{I_{r,orf}(2T_{eV,orf})}_{\text{Electron heating}} = H_{base} + H_{ins} + H_{rad} \quad (2.40)$$
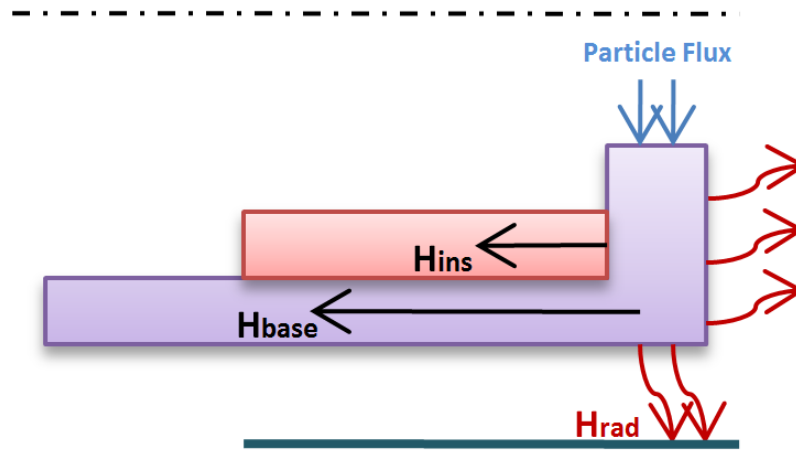
Figure 2.5. Orifice wall energy fluxes.

In Equation 2.40, H_{base} stands for the amount or heat that is lost to base by conduction, H_{ins} represents the amount of heat that is lost to insert by conduction and H_{rad} is the amount of heat that is lost by radiation. In ion heating term, ions deliver the ionization energy, the energy gain while passing through sheath and the kinetic energy to the orifice wall. Since the sheath creates a retarding potential for electrons, the electrons which carry sufficient energy to overcome this retarding sheath potential can reach the orifice surface. $2T_{eV,orf}$ term in electron heating accounts the energy transferred to the orifice wall by electrons.

3. SOLUTION OF MODEL EQUATIONS

In this section, the solution methodology of the insert and orifice plasma model equations explained in previous section is given. The details regarding the solution of the model equations and lifetime calculation of orificed hollow cathode can be found in this section. The results obtained with the developed model are shared in the next section.

The reference geometry modelled in this study is adopted from [45] and is shown in Figure 3.1. Basically, there are three main geometric parameters that are associated with the hollow cylindrical insert: the inner diameter, $D_{in} = 3$ mm, the outer diameter, $D_{out} = 6.9$ mm, and the length $L_{ins} = 6$ mm. Length of the orifice and its diameter are $L_o = 0.36$ mm, $D_o = 0.3$ mm, respectively. Lastly, the total length of the cathode tube is $L_{tube} = 20$ mm. The thickness of the cathode tube is taken as 0.3 mm.
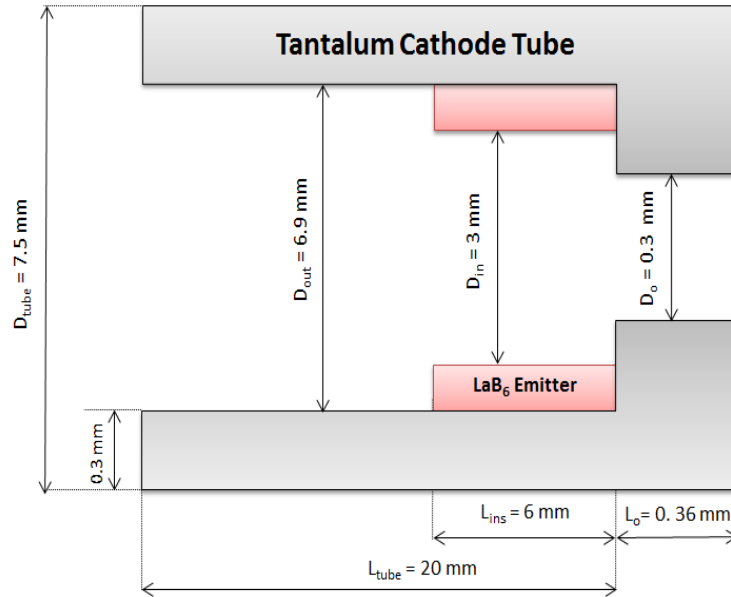
Figure 3.1. Test geometry.

The heat transfer coefficient of the cathode tube material and insert material must be known in order to perform heat transfer calculations. The thermal conductivity of LaB_6 insert material is taken as $k_{ins} = 130 \ W/m \cdot K$ [59]. The cathode tube is assumed to be made of tantalum, thus $k_t = 63 \ W/m \cdot K$ [60]. The thermal conductivity of BaO-W

emissive material is assumed to be the same as that of tungsten. Therefore, the thermal conductivity of BaO-W is taken as 107 $W/m \cdot K$ [60]. Cathode base temperature is assumed to be constant at 1000 K, and the temperature of the radiation shield is assumed to be constant at 1200 K for the heat transfer calculations. The change of the thermal properties of the materials due to temperature variations are ignored. Since hollow cathode operates in vacuum environment, there is no heat loss with convection from insert or orifice. The view factor, used in radiation heat loss calculations, is taken as unity. The cathode is operated at discharge currents varying from 0.5 A to 3 A with 0.5 A increment and at xenon flow rates of 0.3 mg/s, 1 mg/s and 2 mg/s. The equations used in the developed model for simulation of insert and orifice region plasmas are summarized below:

Insert plasma model equations:

- Ion conservation equation:

$$q\pi r_e^2 L_{emit} N_e n_e \langle \sigma v_e \rangle = J_{i,Th}\left(\pi r_e^2\right) + J_{i,Bohm}\left(2\pi r_e L_{emit} + \pi r_e^2\right) \quad (3.1)$$

- Energy conservation equation:

$$I_{em}\phi_s + R_e I_d^2 = I_{i,out}\left(U_i + \frac{2k_B T_{w,ins}}{q}\right) + \left(2T_{eV,ins} + \phi_s\right)I_r + \frac{5}{2}T_{eV,ins}I_d \quad (3.2)$$

- Current balance equation:

$$I_{em} + I_i = I_d + I_r \quad (3.3)$$

Orifice plasma model equations:

- Ion conservation equation:

$$\left(\frac{r_o}{\lambda_{01}}\right)^2 N_o \sigma_i\left(T_{e,orf}\right)\sqrt{\frac{8k_B T_{e,orf}}{\pi m_e}} = \frac{q}{m_i}\frac{T_{iV,orf} + T_{eV,orf}}{\sigma_{cex}N_o}\sqrt{\frac{m_i}{k_B T_{i,orf}}} \quad (3.4)$$

- Energy balance equation:

$$R_o I_d^2 = \left(q\pi r_o^2 L_o N_o n_o \langle \sigma v_e \rangle\right)(U_i) + 2.5\frac{k_B}{q}I_d\left(T_{e,orf} - T_{e,ins}\right) \qquad (3.5)$$

- Orifice wall energy balance:

$$I_{Bohm,orf}\left(U_i + \phi_{s,orif} + 0.5\frac{k_B T_{w,orf}}{q}\right) + I_{r,orf}(2T_{eV,orf}) = H_{base} + H_{ins} + H_{rad}$$

$$(3.6)$$

Bisection method is used for solution of the ion and energy conservation equations written for both insert and orifice region plasmas. Since the temperature of neutral particles in the orifice region plasma is required for calculation of the insert plasma pressure and consequently for calculation of the effective emission length of insert material, orifice plasma neutral particle temperature is taken as 1500 K for the first discharge current value (0.5 A). Orifice plasma neutral particle temperature is updated for the subsequent values of the discharge current.

For the solution of emitter region plasma parameters, the emitter wall temperature is varied. First, the emitter plasma ion conservation equation, Equation 3.1, is solved using bisection method in order to obtain the emitter plasma electron temperature, $(T_{eV,ins})$. After that, insert plasma energy balance equation, Equation 3.2, is also solved with the same method in order to have the emitter plasma electron density, (n_e). Iteration of emitter wall temperature is terminated when the current balance equation, Equation 3.3, is satisfied. For determining whether the current balance equation is satisfied, all the terms in the current balance equation (Equation 3.3) are written on the left hand side of the equality and set equal to zero. As the insert wall temperature is iterated, the calculated value of the insert wall temperature is determined as the current balance equation (Equation 3.3) is satisfied with a relatively small error on the order of 2 %. It is to author's knowledge that the accuracy of the emitter wall temperature prediction can be increased by increasing the resolution of emitter wall temperature iteration.
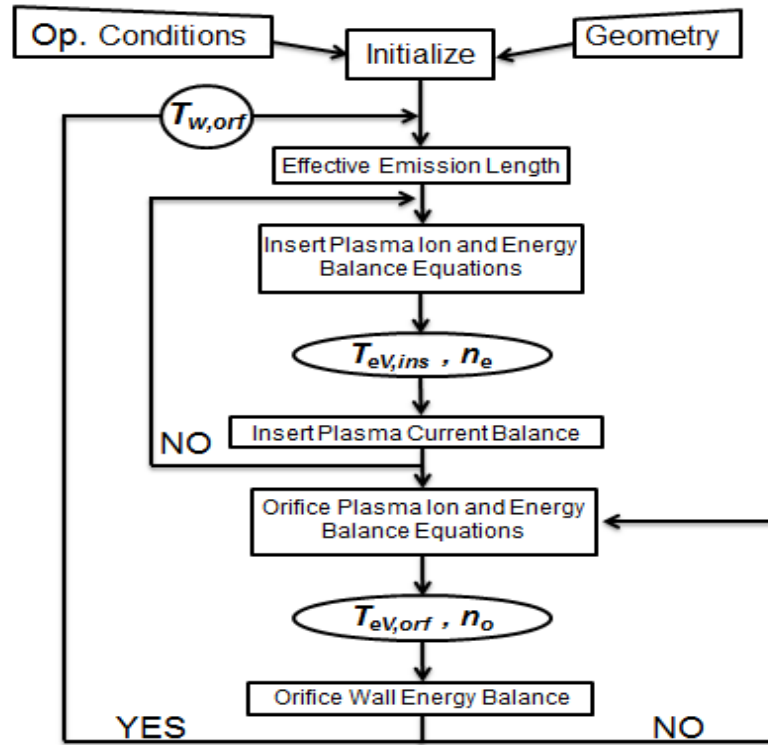
Figure 3.2. Flow chart of the global model for OHC.

The same logic is applied for the orifice region plasma. While the orifice wall temperature is varied, ion conservation equation, Equation 3.4, and orifice plasma energy balance equation, Equation 3.5, are solved consecutively with bisection method in order to obtain the orifice plasma electron temperature, $(T_{eV,orf})$, and plasma density, (n_o). Iteration of orifice wall temperature is terminated when energy balance equation written for the orifice wall, Equation 3.6, is satisfied. Flow chart diagram of the solution procedure can be seen in Figure 3.2.

As a first order approximation, lifetime of hollow cathode can be estimated by evaporation rate which is a function of current density [14, 26]. Therefore, for lifetime calculation, a mathematical expression, Equation 3.7, is obtained for LaB_6 evaporation rate versus current density using graph given in [14]:

$$W = 3 \times 10^{-11} J_{em}^{(2.564)} \tag{3.7}$$

where J_{em} is the electron emission current density in A/cm^2 and W is the evaporation

rate in $gm/cm^2 s$. Lifetime of insert is calculated as the time required to halve the initial mass of emitter material [45]. It should be noted that this approximation for lifetime determination does not consider any other factors that can affect lifetime significantly, such as poisoning due to impurities in gas being used.

4.   RESULTS AND DISCUSSIONS

In this section, results of the effects of operation conditions and geometry on plasma parameters obtained with the developed code are presented. The propellant gas modelled in this model is pure xenon. The impurities in the propellant gas are not taken into account. The comparisons of the results obtained from the developed model with the other numerical and experimental studies are also shared in the following section.

4.1.   Effect of Operation Conditions

The calculated insert region plasma electron temperature is around 1.03 eV. The results show that the electron temperature slightly increases with increasing discharge current for a given flow rate. It is also found that the emitter plasma electron temperature is an increasing function of mass flow rate. However, this variations are small, as also shown in [61]. As shown experimentally in studies [62, 63] and theoretically found in [34, 61] insert wall temperature is an increasing function of discharge current. Furthermore, at a given discharge current, emitter wall temperature shows an increasing trend with propellant flow rate as observed by Goebel [64]. As can be seen in Figure 4.1, the emitter wall temperature increases with increasing discharge current and mass flow rate.

The plasma density in the emitter region is plotted in Figure 4.2. The number density of the emitter plasma increases with increasing discharge current. According to experimental [63, 65] and theoretical [66] studies in the literature, insert plasma density has an almost linear dependence on discharge current at a given mass flow rate. The model also captures this linear dependence.

Similar to the emitter wall temperature, orifice wall temperature shows an increasing trend with both discharge current and mass flow rate as shown in Figure 4.3. Predicted orifice wall temperature is lower than insert wall temperature. It is found
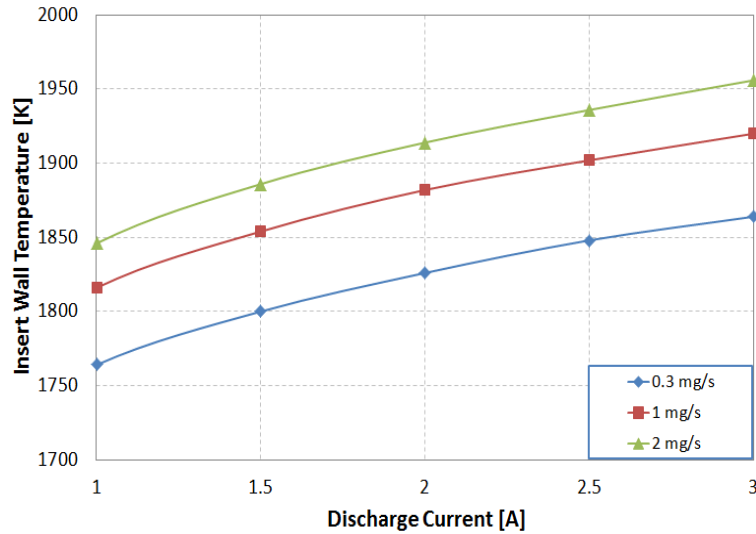
Figure 4.1. Insert wall temperature as a function of discharge current.
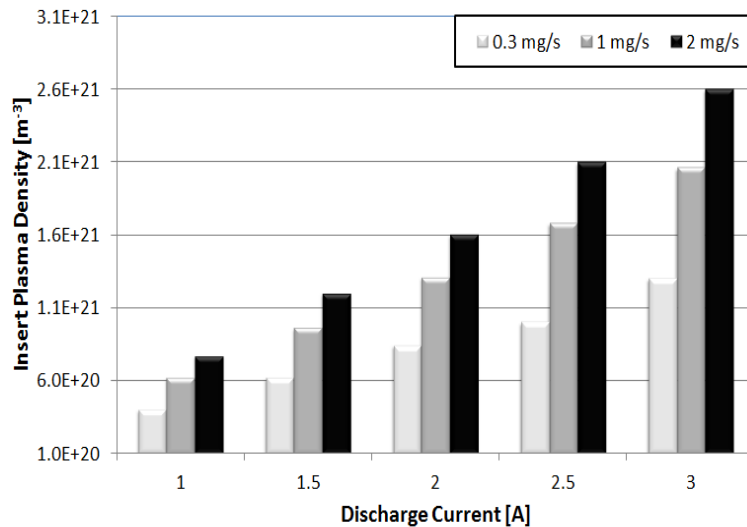
Figure 4.2. Emitter plasma density as a function of discharge current.

in experimental studies [13, 67] conducted with hollow cathodes having BaO-W insert that orifice plate temperature could be up to 100°C cooler than insert temperature.

As was the case for emitter, it is found that the orifice plasma density is also an increasing function of both discharge current and mass flow rate as seen in Figure 4.4.

The electron temperature of the orifice region remains almost constant with discharge current whereas it decreases with the propellant flow rate as shown in Figure 4.5 and as found by Domonkos [34].
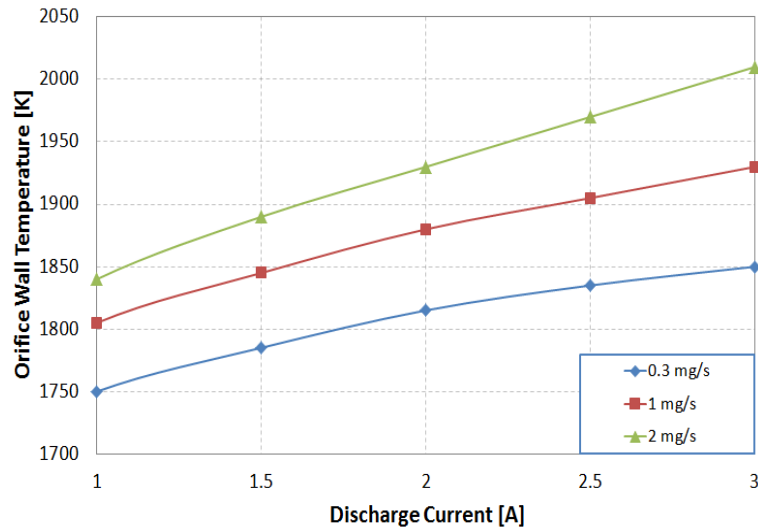
Figure 4.3. Orifice wall temperature as a function of discharge current.
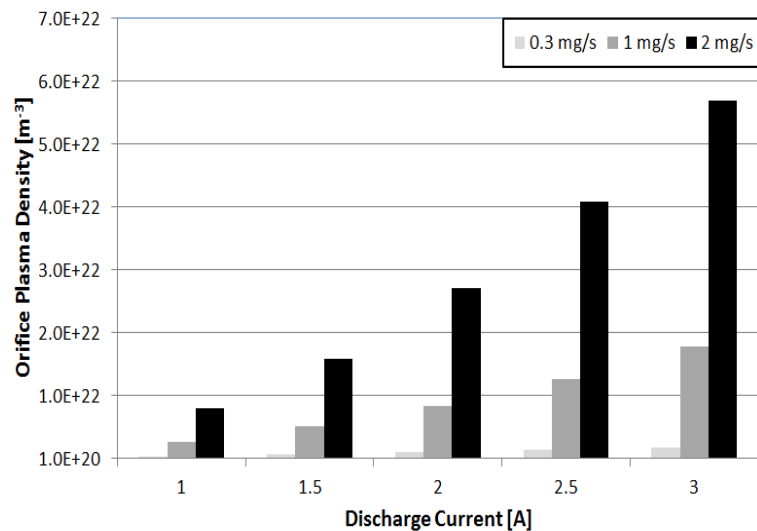
Figure 4.4. Orifice plasma density as a function of discharge current.

Insert lifetime has a decreasing tendency with both discharge current and mass flow rate as seen in Figure 4.6 which is consistent with lifetime result of Alta model [45]. Here, it should be noted that, even tough the same procedure is applied for prediction of insert lifetime, our model calculates shorter lifetime which can be explained by higher emitter wall temperature predicted by our model.

Figure 4.7 shows the NSTAR neutralizer cathode internal pressure values predicted by the model. The predicted results are higher than the experimental values presented in [13]. This higher pressure prediction can be explained by model's overestimation of the orifice wall temperature for NSTAR cathode. However, it is found that
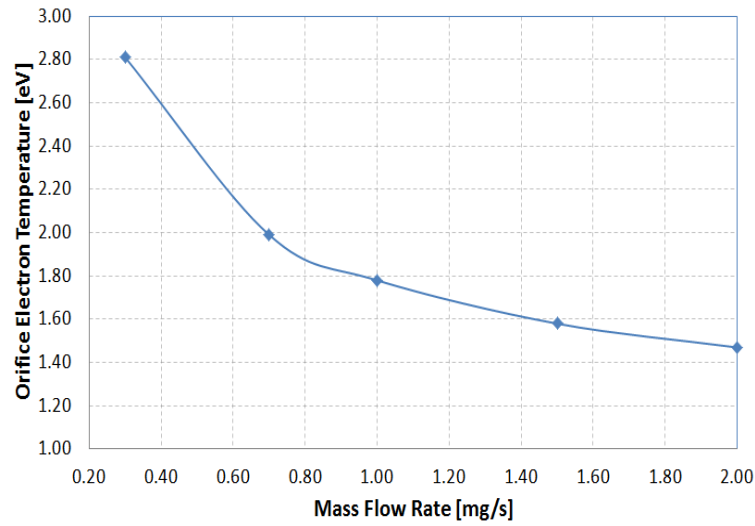
Figure 4.5. Orifice electron temperature as a function of mass flow rate at 2 A discharge current.
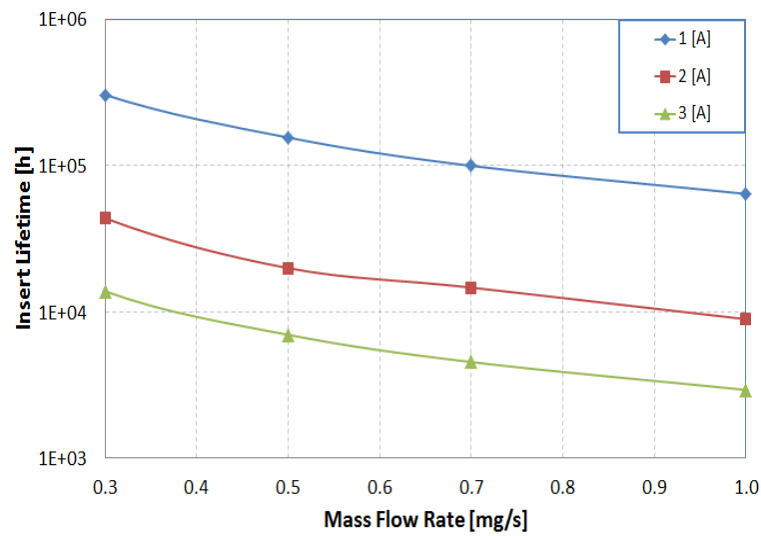
Figure 4.6. Insert lifetime as a function of discharge current and flow rate.

the internal pressure of an OHC increases with both flow rate and discharge current which is consistent with experimental results in literature [13].

4.2. Effect of Geometry

At 1 mg/s xenon flow rate and 2 A discharge current, the influence of the geometry on the cathode has also been studied. According to Figure 4.8, the insert temperature is a decreasing function of the insert inner diameter which shows an agreement with
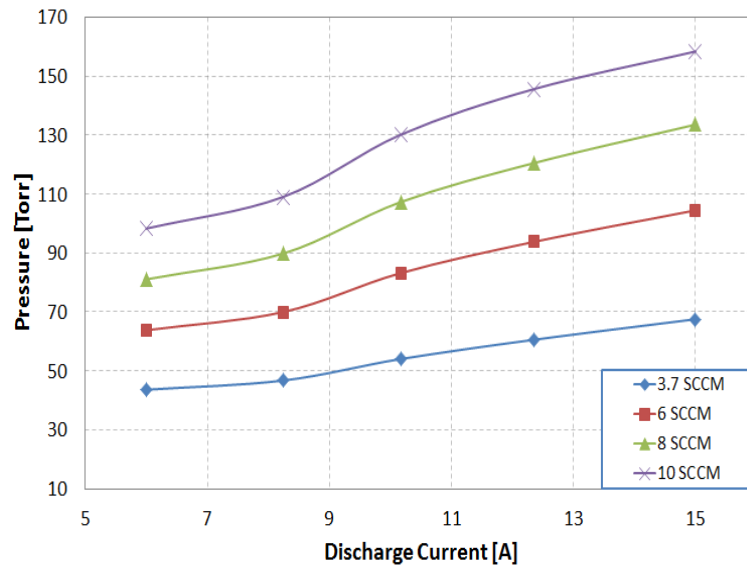
Figure 4.7. NSTAR neutralizer cathode internal pressure as a function of flow rate and discharge current.

the results of Domonkos' model [34]. As proposed in study [68], increase in insert inner diameter increases the effective emission area of insert material and thus reduces the insert wall temperature. As given in Figure 4.9, this behaviour of hollow cathode is captured by developed model. Figure 4.9 shows that increase in insert inner diameter increases the effective emission length of emitter material. Increasing the effective emission length of emitter material reduces the current density emitted from insert. Therefore, insert temperature decreases. In other words, the same amount of current can be obtained at lower emitter wall temperatures.

Another finding from the model is that the wall temperature of the insert decreases with the orifice diameter as seen in Figure 4.10. Similarly, increasing the orifice diameter increases the effective emission length and consequently reduces the wall temperature of insert as found in [4]. The change in effective emission length of insert material with orifice diameter is given in Figure 4.11. It is calculated by the developed model that insert effective emission length increases with increasing the diameter of orifice.

Effect of orifice length on insert temperature is also studied. Insert wall temperature increases with orifice length as shown in Figure 4.12. This increase in insert
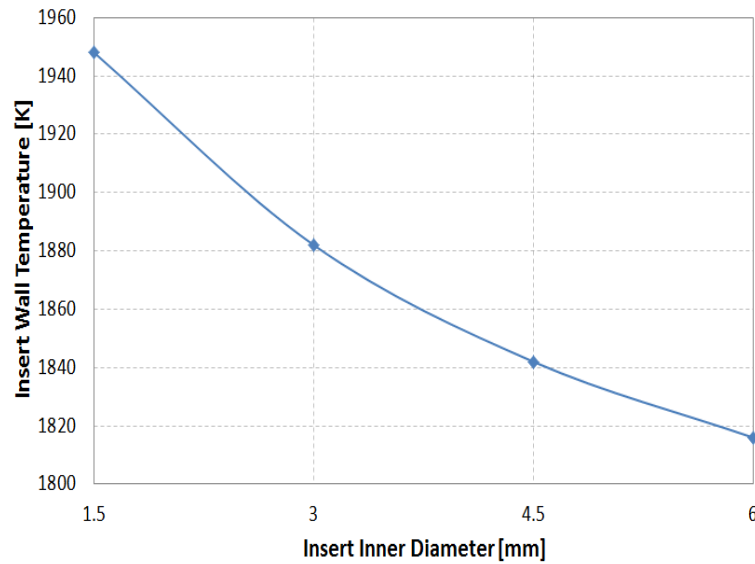
Figure 4.8. Insert temperature as a function of insert inner diameter.

wall temperature can be attributed to decrease in effective emission length with orifice length. As show in Figure 4.13, increasing the orifice length decreases the effective emission length of emitter.

For a given flow rate and orifice diameter, Mandell and Katz [36] predicts an increase in the orifice plasma electron temperature, as a result of ohmic heating, when the orifice length is increased. Elevated electron temperature enhances the ionization in the orifice plasma, and the electron and ion fluxes to the walls of the orifice increases. Thus power deposition to the orifice wall due to ion heating and electron heating, represented in brackets in Equation 2.40, increases. As a result, orifice wall temperature also increases with orifice length as seen in Figure 4.14. Figure 4.15 shows the amount of power transferred from particles striking to the wall of orifice, with respect to orifice length. Since plasma density and sheath potential is high in the orifice plasma, the heating mechanism of the orifice wall is mainly due to ion heating [69].

Lifetime of insert with respect to orifice length is given in Figure 4.16. Insert lifetime decreases with increasing orifice length. As we have already shown, increasing the orifice length decreases the effective emission length of emitter which leads higher current density emission from insert material. Since the lifetime of LaB_6 is mainly dependent on current density, insert lifetime decreases with orifice length.
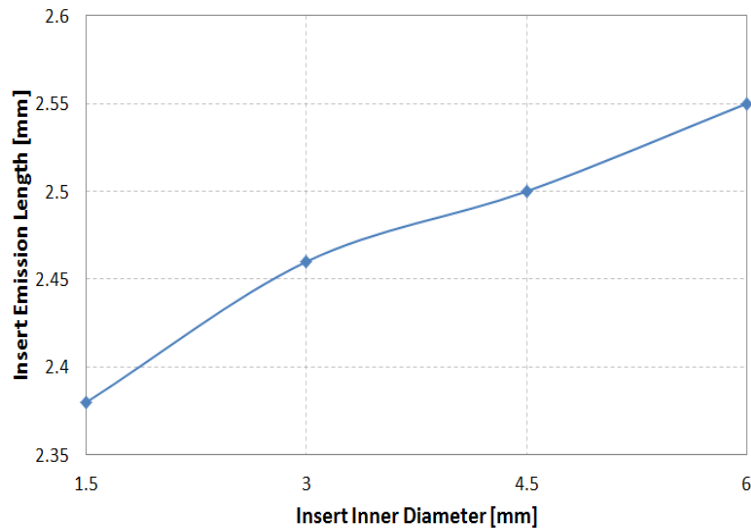
Figure 4.9. Insert effective emission length as a function of insert inner diameter.
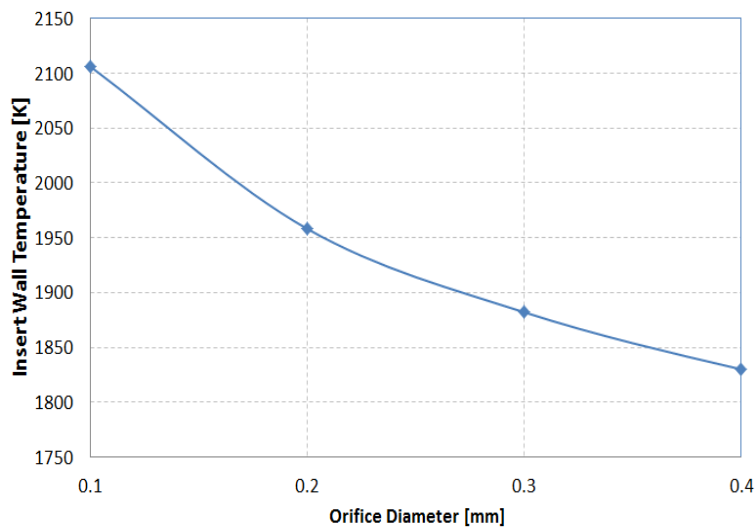
Figure 4.10. Insert temperature as a function of orifice diameter.

Hollow cathodes, which have large aspect ratio (L_o/D_o), in other words small orifice diameter for a given length, have high internal pressure. Ion bombardment of the orifice wall becomes significant in large aspect ratio cathodes [50]. Keeping the orifice length at 0.3 mm, the orifice diameter is varied and the effects of orifice diameter on orifice wall temperature is modelled as well. As given in Figure 4.17, the developed model calculates an increase in orifice wall temperature with decreasing orifice diameter. Decrease in orifice diameter increases the power deposition to the walls of the orifice and as a consequence, orifice wall temperature increases. As plotted in Figure 4.18, heating of orifice wall with electron and ion flux increases. As the orifice
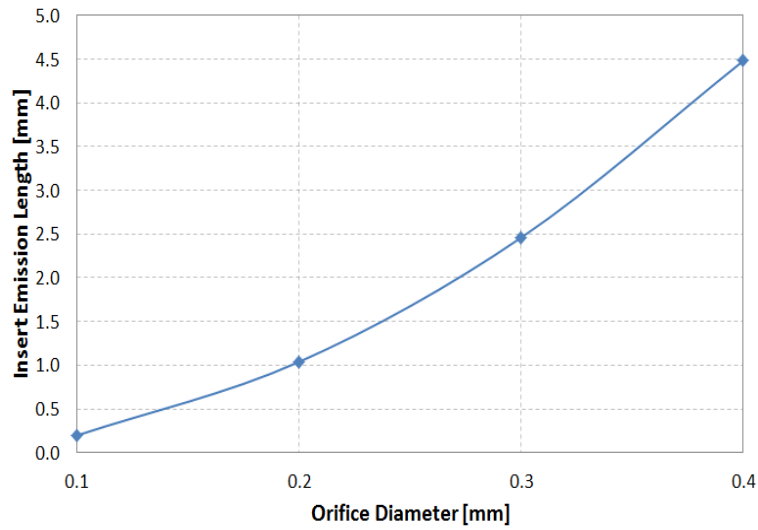
Figure 4.11. Insert effective emission length as a function of orifice diameter.
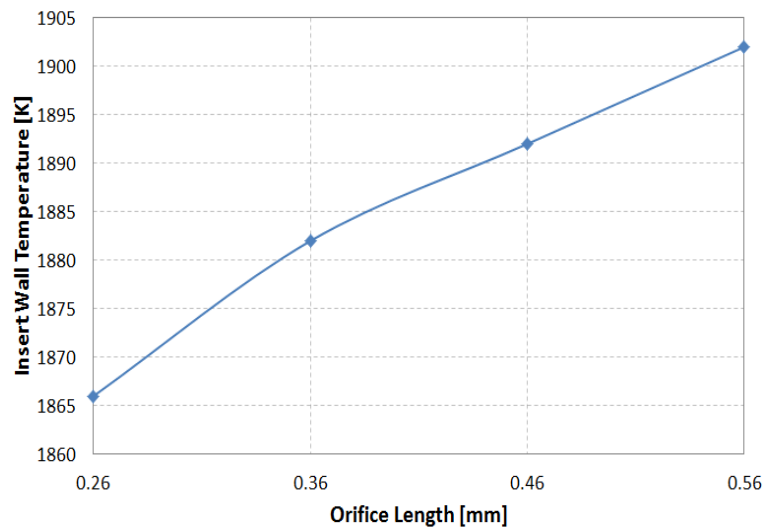
Figure 4.12. Insert wall temperature as a function of orifice length.

diameter decreases, ion heating becomes significant.

Aside from increasing the orifice wall temperature, decreasing the orifice diameter also increases the insert plasma pressure as shown in Figure 4.19.

The effect of the thickness of the cathode tube on orifice wall temperature is plotted in Figure 4.20. Increasing the thickness of the cathode tube wall increases the heat conduction from orifice to the cathode base therefore, the thicker the cathode tube, the lower the orifice wall temperature is. Even tough it is expected that thicker cathode tube decreases the temperature of the emitter, the developed model does not
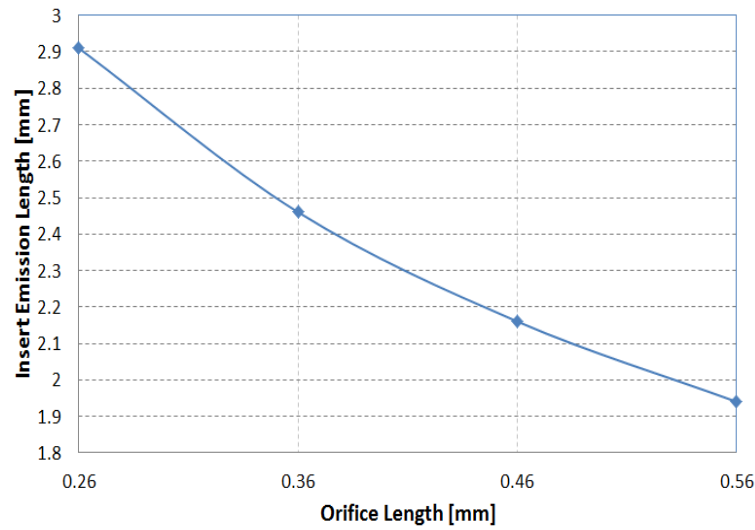
Figure 4.13. Insert effective emission length as a function of orifice length.
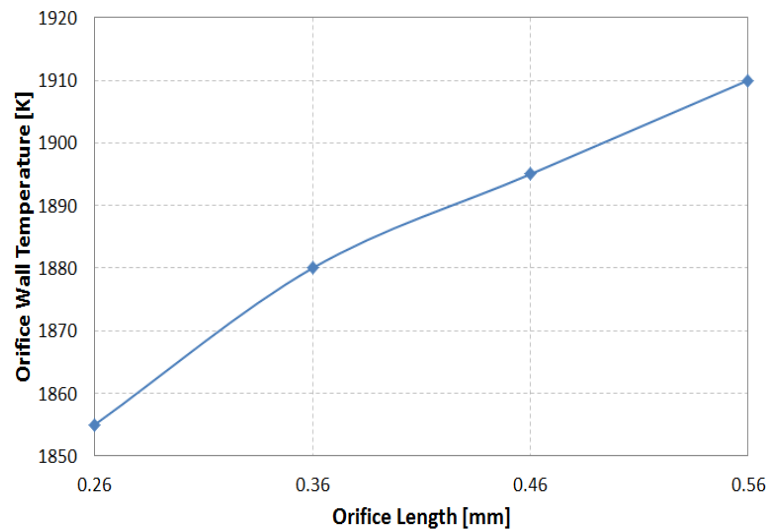
Figure 4.14. Orifice wall temperature as a function of orifice length.

calculate any difference which can be considered as a shortcoming of the model.

The power consumption of the OHC is also modelled with the developed global model. The power consumption is assumed to be the combination of three contributions: the consumption due to voltage drop at the insert sheath, the consumption due to ohmic heating of the insert plasma and the consumption due to ohmic heating in the orifice plasma. The effect of discharge current on power consumption is investigated at 1 mg/s xenon flow rate. The power consumption at three different discharge current values is given in Figure 4.21. The power consumption increases with discharge current because of the increased ohmic heating of the plasmas in both regions, as well as the
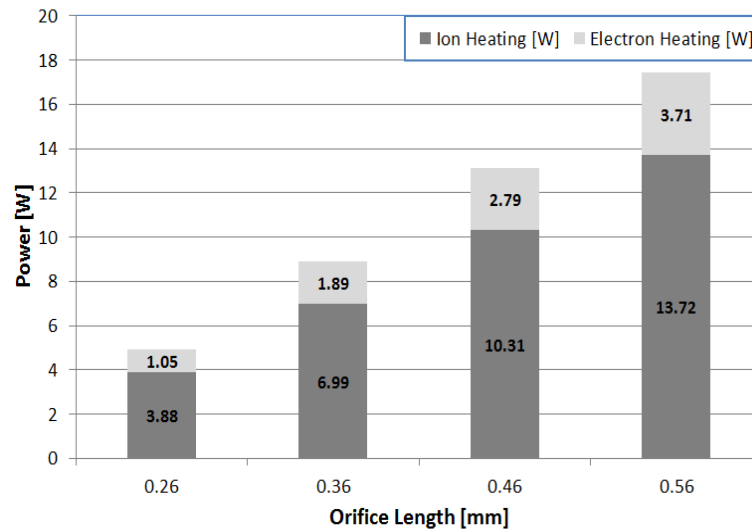
Figure 4.15. Amount of power delivered to orifice wall as a function of orifice length.
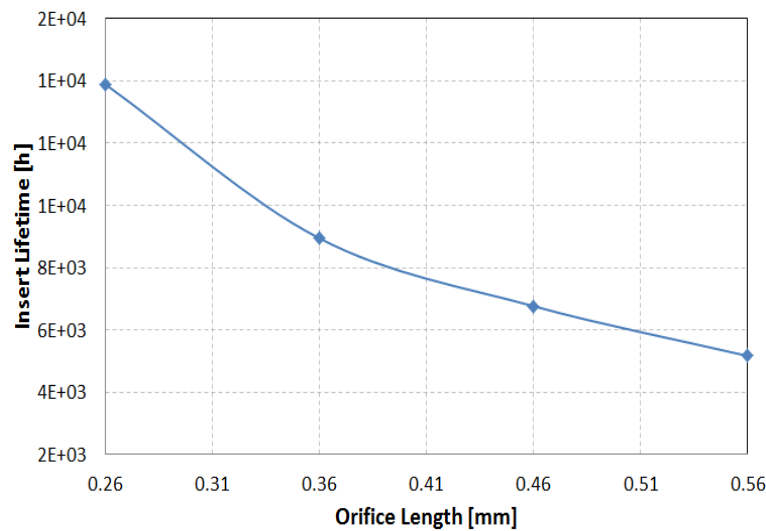
Figure 4.16. Insert lifetime as a function of orifice length.

increase of the voltage drop on emitter sheath.

As suggested by Domonkos with both experimental and theoretical investigations [34], the insert diameter should be large in order to reduce the power consumption. The effect of the insert inner diameter on power consumption is given in Figure 4.22. It is obtained with the developed model that power consumption increases with the insert inner diameter. This increase in power consumption with the increase in insert inner diameter is not consistent with the findings of Domonkos [34].

Figure 4.23 displays the effect of orifice diameter on power consumption. The
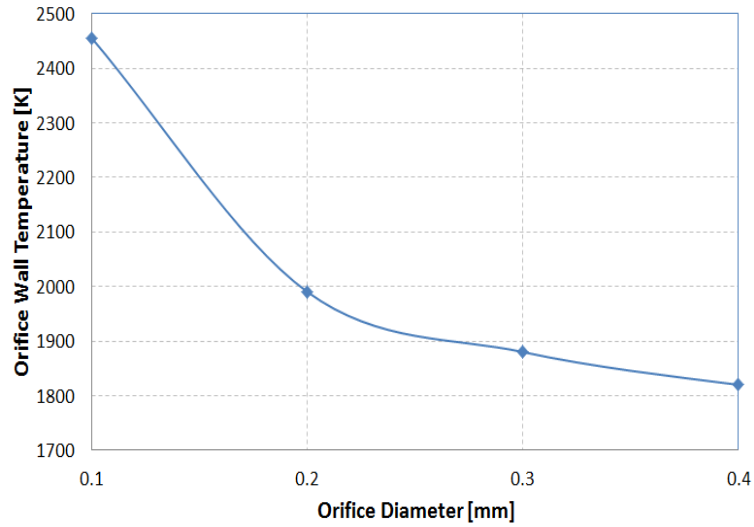
Figure 4.17. Orifice wall temperature as a function of orifice diameter.
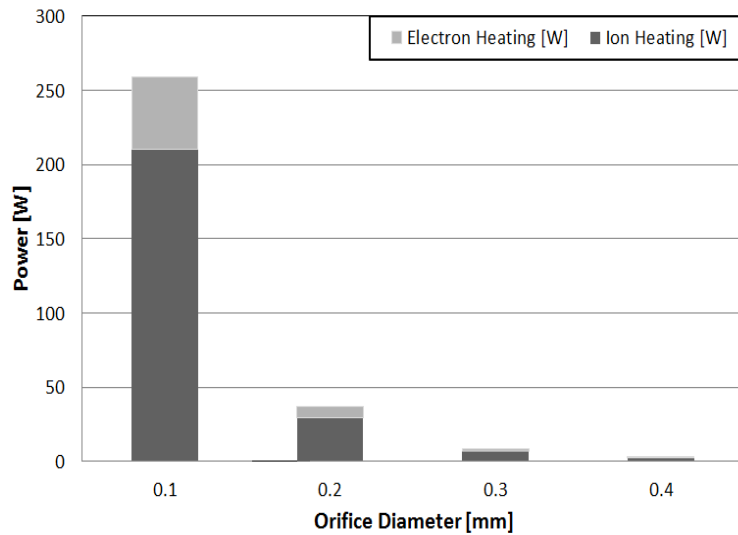
Figure 4.18. Amount of power delivered to orifice wall as a function of orifice diameter.

resistance of orifice plasma increases as expected. The decrease in orifice diameter also increases the resistive heating of insert plasma because the insert plasma electron density increases as shown in [34] and effective length decreases with decreasing the orifice diameter. Hence, the power consumption increases with decreasing the orifice diameter.

The effect of orifice length on power consumption is also investigated. As shown in Figure 4.24, power consumption increases with orifice length. The power consumption due to orifice and insert plasma resistance increases with orifice length, whereas the
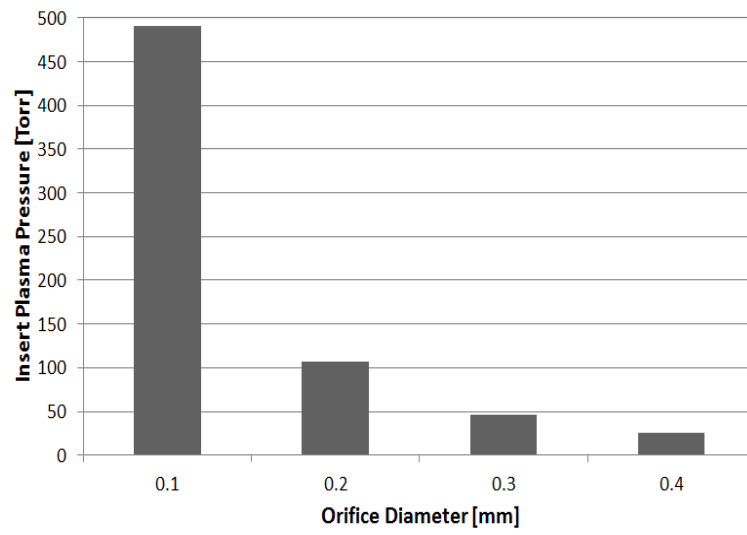
Figure 4.19. Insert plasma pressure as a function of orifice diameter.
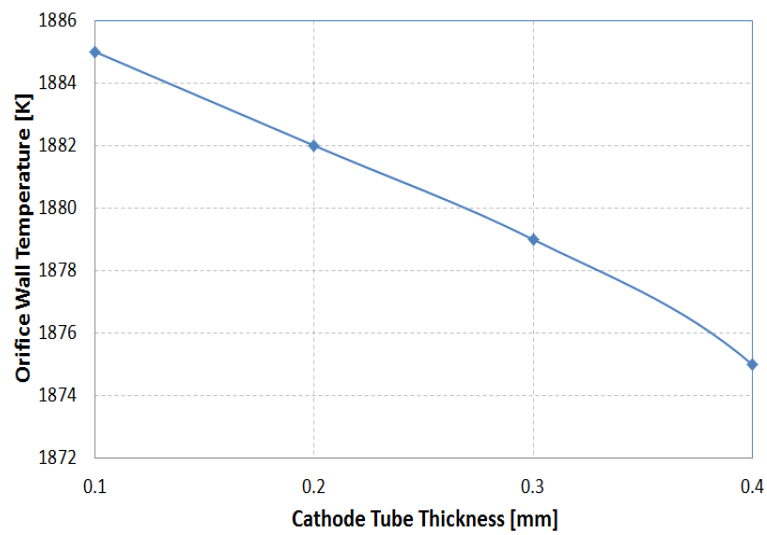
Figure 4.20. Orifice wall temperature as a function of cathode tube thickness.

power consumption due to emitter sheath voltage drop remains almost constant.
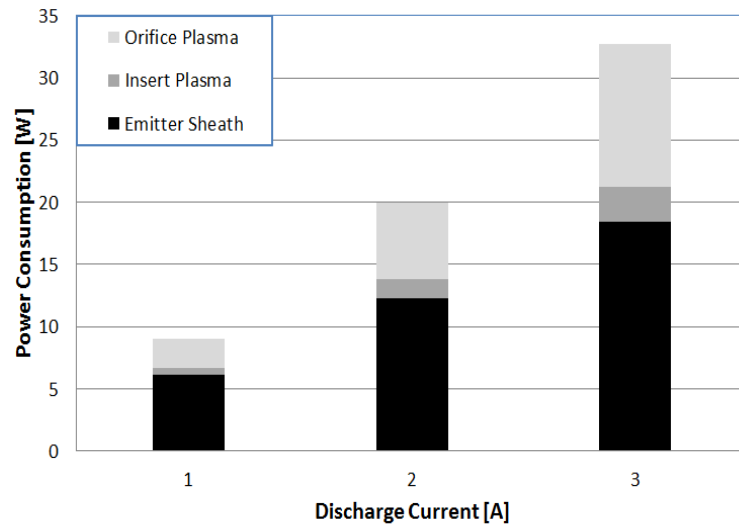
Figure 4.21. Power consumption as a function of discharge current.
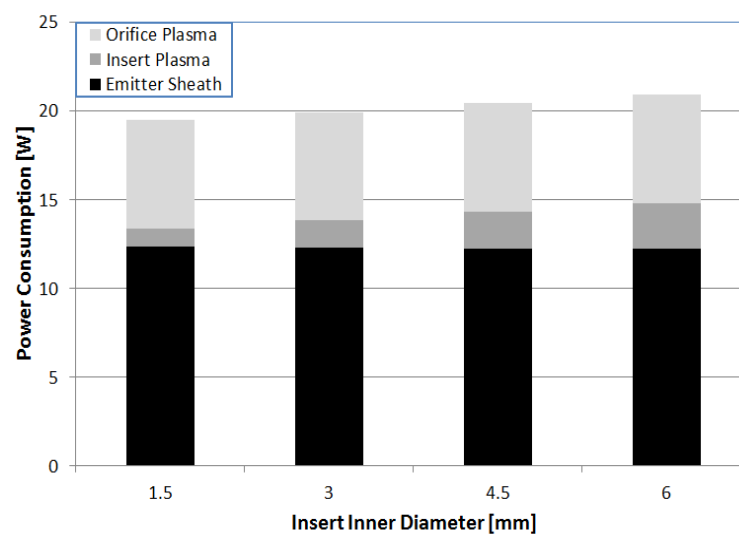
Figure 4.22. Power consumption as a function of insert inner diameter.
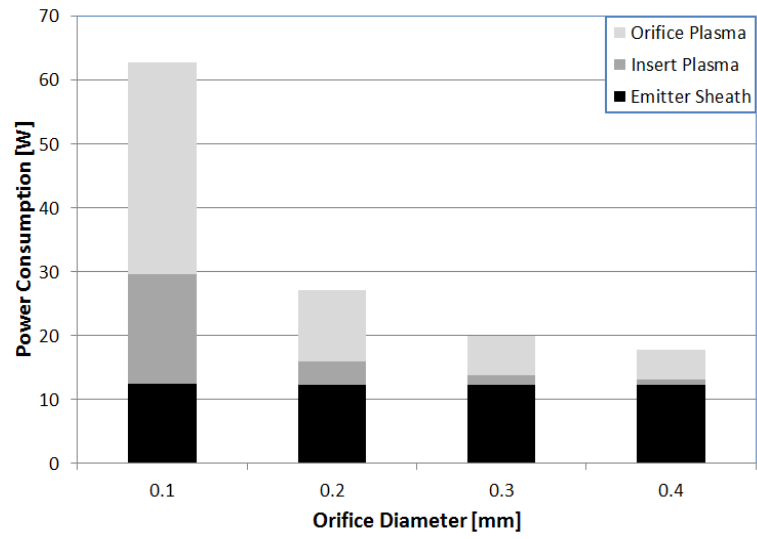
Figure 4.23. Power consumption as a function of orifice diameter.
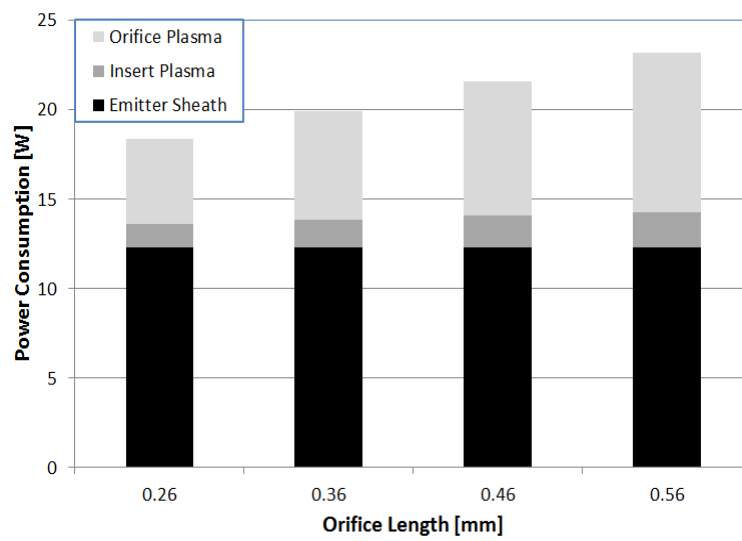
Figure 4.24. Power consumption as a function of orifice length.

5. COMPARISON WITH EXPERIMENTAL AND NUMERICAL STUDIES

For further comparison, calculated insert temperatures, at 0.3 mg/s xenon flow rate, obtained with Alta model [45] and our model are shown in Figure 5.1. Model gives higher emitter temperatures compared to Alta model. Insert temperature prediction of the model for NSTAR neutralizer cathode is also compared with the experimental data present in study [13] for different throttle points (TH4, TH8, TH11, TH14 and TH15). The operation parameters at different throttle points can be seen in Table 5.1. As seen in Figure 5.2, the model calculates lower temperature. The difference between prediction and experiment increases with higher throttle levels.
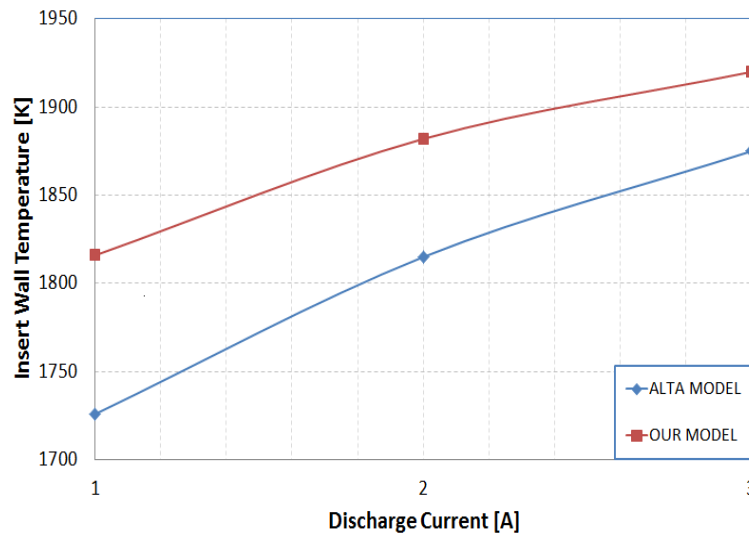
Figure 5.1. Comparison of calculated insert wall temperatures at 1 mg/s.

Comparison of predicted orifice wall temperature with Alta model is shown in Figure 5.3. With increasing discharge current, difference between orifice wall temperature predictions of the two models gets closer. Similarly, our model predicts higher orifice temperature in comparison with Alta model.

The comparisons of predicted insert and orifice wall temperatures with Alta model at 0.3 mg/s are also given in Figure 5.4 and Figure 5.5. As was the case at 1 mg/s, the developed model predicts higher insert and wall temperature in comparison to Alta

Table 5.1. NSTAR neutralizer cathode throttle levels [13].

NSTAR Throttle Level	Discharge Current [A]	Flowrate [sccm]
TH 4	6.0	2.47
TH 8	8.24	2.47
TH 11	10.17	2.73
TH 14	12.35	3.34
TH 15	15.0	3.70
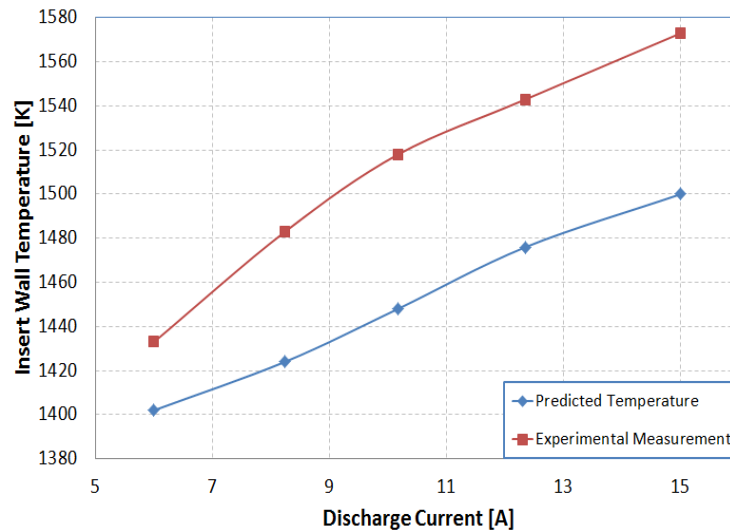
Figure 5.2. Comparison of predicted NSTAR insert temperature with experimental measurement [13].

model. Similar to the case at 1 mg/s, with increasing discharge current, difference between orifice wall temperature predictions of the two models gets closer.

A more comprehensive comparison study with other numerical studies present in the literature is conducted. NSTAR neutralizer cathode, which has an orifice 0.75 mm in length and 0.28 mm in diameter and a barium-oxide impregnated tungsten insert material, operated at 3.6 sccm xenon flow rate and 3.26 A discharge current is simulated by developed code and comparison of results obtained with the same geometry and operation conditions are given in Table 5.2. Here, it should be noted that in 0-D models developed by Katz and Mandell [43] and Mizrahi and Vekselman [44] energy
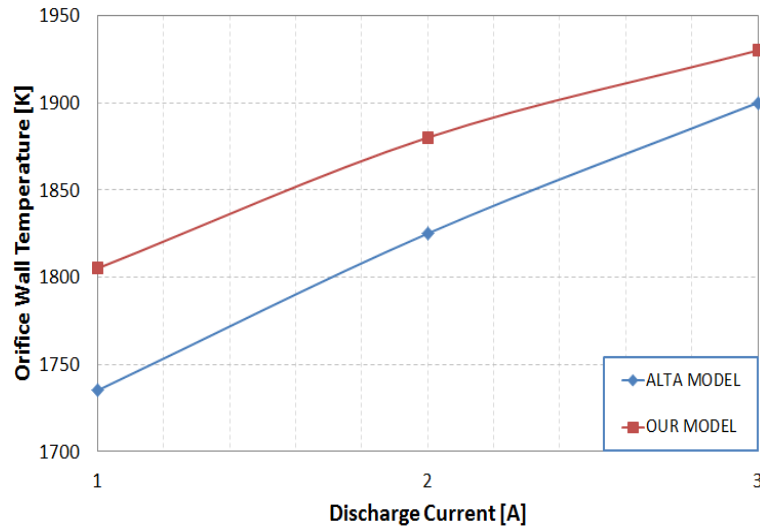
Figure 5.3. Comparison of calculated orifice wall temperatures at 1 mg/s.
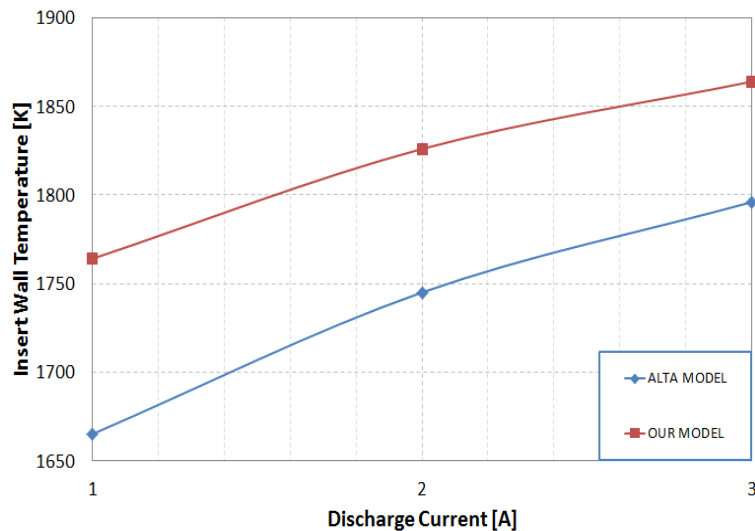
Figure 5.4. Comparison of calculated insert wall temperatures at 0.3 mg/s.

losses due to excitation processes are taken into account in plasma energy balance equation whereas in our model it is neglected. From the viewpoint of 0-D models, our model predicts higher electron temperature in orifice plasma in comparison to Katz and Mandell [43], and Mizrahi and Vekselman [44] whereas lower than the Alta model [45]. Calculated plasma density is lower than that predicted by [43] and [44]. Predicted neutral particle density in orifice plasma is lower than the prediction of [44] and higher than other 0-D models. Even tough neutral particle density calculated by our model is higher, plasma density and plasma temperature results are in a good agreement with orifice outlet results of the 2-D model developed by Mikellides and Katz [70].
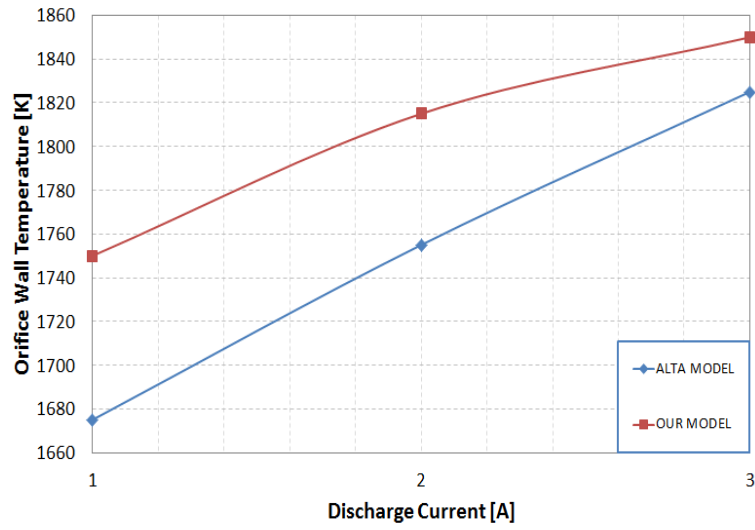
Figure 5.5. Comparison of calculated orifice wall temperatures at 0.3 mg/s.

Table 5.2. Comparison of results obtained from different numerical models for NSTAR neutralizer cathode [45].

	Our Model	Alta	Mizrahi Vekselman	Katz Mandel	Mikellides Katz
Plasma Parameters	Average	Average	Average	Average	Orifice Outlet
N_o $[10^{23}\ m^{-3}]$	0.6	0.2	1.1	0.4	0.1
n_o $[10^{22}\ m^{-3}]$	0.7	0.7	2.7	1.0	0.5
$T_{eV,orf}$ [eV]	2.4	2.7	1.6	2.2	2.2
$\frac{n_o}{n_o+N_o}$	0.10	0.24	0.2	0.18	0.33

6. CONCLUSIONS

A global numerical model for orifice and insert regions of a typical orificed hollow cathode operating with LaB_6 thermionic emitter and xenon propellant is developed under the assumption of the presence of a quasi-neutral plasma with uniform plasma parameters in both regions. The conservation and balance equations written for insert and orifice plasmas are solved to have the plasma parameters and to assess the effect of geometry on both plasma regions. Furthermore, the comparison of the obtained results with other numerical and experimental studies present in the literature are given. The agreement of the obtained results with experimental and numerical studies shows that this indigenous global model can be used for designing more efficient and longer life time hollow cathodes.

Operation at high discharge current and mass flow rate cause the predictions of model to diverge from other results. For instance, the model overestimates orifice wall temperature and internal pressure at high mass flow rate and discharge current. Nevertheless, predictions of the developed model at low operation conditions (mass flow rate and discharge current) for wide range of geometries are satisfactory. Another shortcoming of the model is that it cannot predict the electrical characteristics of OHCs correctly. Therefore, further improvements are necessary in order to simulate the electrical characteristics of OHCs as well.

Having a broader plasma density profile along the insert is crucial in order to increase the lifetime of hollow cathodes. Broader axial plasma density profile in the insert region leads to better plasma-emitter contact and thus increases the emitting surface area of insert material. In other words, better plasma-emitter contact area leads to low current densities and low insert temperatures. Since the lifetime of insert material is mainly determined with its evaporation rate, which depends on the temperature of the material, reduced insert temperatures can guarantee longer lifetime for hollow cathodes. Therefore, in design process of a thermionic hollow cathode, special attention should be paid to insert temperature.

In literature, there are many different studies, efforts and recommendations for extending the lifetime of hollow cathode by increasing its emission length. In 2006, Van Noord [68] suggested increasing the thickness of hollow cathode tube walls. Thicker tube walls will increase the heat conduction and eventually temperature gradient on insert surface can be reduced. Decreasing the temperature variations along the insert material can ensure more uniform thermionic electron emission and consequently extend the lifetime of cathode. In this study, it is observed that thicker cathode tube wall can increase the plasma-emitter contact area. However, since the main energy loss of cathode is heat conduction to the base, it is not desirable to have thicker wall. Rather, thinner and longer cathode tube is used in construction of hollow cathodes [4, 14].

Another method proposed by Van Noord [68] to increase the effective emission length of insert material is increasing the insert inner diameter. It is found in [68] that increasing the insert inner diameter increases the lifetime.

Another suggestion to increase the effective emission length of insert material is to increase the orifice diameter [4]. Increasing the orifice diameter broadens the axial density profile of insert plasma. Therefore, effective emission length increases.

Rather than playing with the cathode geometry and dimensions, attachment of RF coils near the heater coils is another way for increasing the emission length [71]. The main reason for adding RF coil is to deposit RF energy and extend the axial plasma density profile towards the downstream. Extended axial plasma profile increases the plasma emitter contact area and thus reduces the current density.

According to the result of the developed model, increasing the insert inner diameter leads to a decrease in insert wall temperature, due to an increase in effective emission length of insert material, and thus to a higher lifetime as shown in [68]. Another finding is that increasing the diameter of orifice can also increase the lifetime. With increasing the orifice diameter, effective emission length of insert material increases and thus, insert temperature decreases. The prediction of the effect of orifice diameter on insert wall temperature is consistent with the findings of Goebel and Watkins [4]. Fur-

thermore, larger orifice diameter can eliminate the difficulties regarding the discharge initiation from hollow cathode by increasing the penetration of the potential applied by keeper.

The results of the developed model show that reducing the orifice diameter causes a considerable increase in power deposited to the orifice wall and as a consequence increases the orifice wall temperature. The developed model captures the effect of the cathode tube thickness on the orifice wall temperature. The increase in the cathode tube thickness reduces the temperature of the orifice wall. Unfortunately, effect of cathode tube thickness on insert wall temperature cannot be captured by the model, since the insert model does not include heat transfer considerations.

Even though it is shown in study [26] that longer lifetimes can be obtained by using larger sized hollow cathodes, it is found that reducing the length of the orifice is advantageous for maintaining lower insert temperatures and thus longer lifetimes.

APPENDIX A: NEUTRAL PARTICLE DENSITY AND PRESSURE ESTIMATION OF INSERT PLASMA

In the viscous regime, the pressure in a cylindrical tube is determined by Poiseuille flow that is modified for compressible gas [11]. The mole flow rate in moles per second of the compressible gas is given as:

$$N_m = \frac{\pi}{8\zeta} \frac{r^4}{l} \frac{P_a (P_1 - P_2)}{R_g T} = \frac{\pi}{16\zeta} \frac{r^4}{l} \frac{P_1^2 - P_2^2}{R_g T} \quad \left[\frac{1}{\frac{kg}{m \cdot s}} \times \frac{m^4}{m} \times \frac{kg^2}{m^2 \cdot s^4} \times \frac{1}{\frac{J}{mol \cdot K} K} = \frac{mol}{s} \right]$$
(A.1)

where r is the radius and l is the length of the tube, ζ is the viscosity, P_1 is the pressure at the upstream end of the tube, P_2 is the pressure at the downstream end of the tube, T is the temperature of the gas, P_a is the average pressure in the tube and it is given as:

$$P_a = \frac{P_1 + P_2}{2}$$
(A.2)

The measured gas flow rate is given by the ideal gas law:

$$Q = P_m V_m = N_m R_g T_m \quad \left[\frac{mol}{s} \times \frac{J}{mol \cdot K} \times K = \frac{Pa \cdot m^3}{s} \right]$$
(A.3)

where P_m is the pressure, V_m represents the volume, T_m is the temperature and N_m is the mole flow rate [11]. Putting mole flow rate in Equation A.3 gives:

$$Q = \frac{\pi}{16\zeta} \frac{r^4}{l} \frac{P_1^2 - P_2^2}{T} T_m$$
(A.4)

Defining $T_r = T/T_m$:

$$Q = \frac{\pi}{16\zeta} \frac{r^4}{l} \frac{P_1^2 - P_2^2}{T_r}$$
(A.5)

When the necessary unit conversions are done and writing this in terms of gas flow divided by the pressure drop:

$$Q = \frac{1.28d^4}{\zeta T_r l} \left(P_1^2 - P_2^2 \right) \tag{A.6}$$

where Q is the flow rate in terms of sccm, ζ is the viscosity in terms of poise, the pressures are in terms of Torr, d and l are the orifice diameter and orifice length in centimeters, respectively. The pressure at the upstream of the orifice is:

$$P_1 = \left(P_2^2 + \frac{0.78Q\zeta T_r l}{d^4} \right)^{1/2} \tag{A.7}$$

Assuming that P_1 is much higher than P_2, the downstream pressure, P_2, can be neglected. The viscosity of xenon in terms of poise is given as:

$$\zeta = 2.3 \times 10^{-4} T_{r,Xe}^{\left(0.71 + 0.29/T_{r,Xe} \right)} \qquad for \ \ T_{r,Xe} > 1 \tag{A.8}$$

where $T_{r,Xe} = T/293.7$. Once we know the pressure in the cathode interior, the neutral particle density can be calculated in terms of $particles/m^3$ by using ideal gas law:

$$P = Nk_B T \Longrightarrow N = 9.65 \times 10^{24} \times \frac{P}{T} \tag{A.9}$$

APPENDIX B: DERIVATION OF RICHARDSON-LAUE-DUSHMAN EQUATION WITH THERMODYNAMIC APPROACH

The discussion presented here is adapted from [72] and explains briefly the derivation of the Richardson-Laue-Dushman equation. For more detailed explanation, the reader should consult reference [72].

Considering that the electron chemical potential in the vapor is equal to the electrochemical potential of electrons in the conductor, and considering that the relationship between vapor chemical potential and its density is the one which is given by the quantum statistics for a perfect gas with particle in statistical weight, number density of electrons in the vapor that is away from surface is given by:

$$n_1 = \left[2 \left(2\pi m k_B T \right)^{3/2} / h^3 \right] exp \left(\mu_v / k_B T \right) \tag{B.1}$$

where μ_v represents the chemical potential of the vapor and h represents the Planck's constant.

Putting $\bar{\mu} + qM_v$ in place of μ_v in Equation B.1, this equation can be extended to the regions where the image potential is appreciable. Here, M_v is the motive at the given point in vapor. Therefore Equation B.1 becomes:

$$n_1 = 2 \left[\left(2\pi m k_B T \right) / h^2 \right]^{3/2} exp \left(\left(\bar{\mu} + qM_v \right) / k_B T \right) \tag{B.2}$$

The integration over the Maxwellian distribution of electron velocities gives the number of electrons crossing the unit area in either direction in unit time as follows:

$$\Gamma = \frac{1}{4} n_1 \left(\frac{8 k_B T}{\pi m} \right)^{1/2} \tag{B.3}$$

where n_1 is the number of electrons per unit volume in the vapor.

The definition of saturation can be explained as the plane in question is placed at an enough distance away from the surface where it is beyond the maximum in the motive created by the superposition of the applied field and the image field. Assuming that the transition from equilibrium to saturation does not change the state of emitting material, if we follow the path of electrons, it can be seen that some of the electrons enter the interior of the emitter and some crosses the plane. $\bar{r}_v$ represents the fraction of electrons passing across the plane to the total. Here, it is assumed that there are no considerable collisions between vapor electrons in the region between the plane and the emitter which leads that the reflection coefficient, $\bar{r}_v$, is dependent on surface and the field close to it, not dependent on the density of the vapor. Since current density is defined as the product of elementary charge, particle density and particle velocity, combining the reflection coefficient with Equations B.2 and B.3, saturation current density, J, can be obtained as follows:

$$
\begin{aligned}
J &= 2\left[\left(2\pi m k_B T\right)/h^2\right]^{3/2} exp\left(\left(\bar{\mu}+qM_v\right)/k_B T\right) \times \frac{1}{4}\sqrt{\frac{8k_B T}{\pi m}} \times q \times \left(1-\bar{r}_v\right) \\
&= A(1-\bar{r}_v)T^2 exp((\bar{\mu}+qM_v)/k_B T)
\end{aligned}
\tag{B.4}
$$

In Equation B.4, A is the universal constant and has the value:

$$
A = \left(4\pi m k_B^2 q/h^3\right) = 120 \qquad [A/cm^2 K^2]
\tag{B.5}
$$

The true work function, which can be defined as the difference between the electrochemical potential, $\bar{\mu}$, of the electrons in the emitter and the electrostatic potential energy of an electron, $-q\Phi_a$, just outside the conductor, is given as:

$$
\phi = -\Phi_a - \left(\bar{\mu}/q\right)
\tag{B.6}
$$

Considering that if a quite weak field is sufficient to produce saturation, the plane just outside the range has the same potential with the one just outside of the surface of

the emitter and using the Equation B.6, the saturation current density, Equation B.4, reduces to a more familiar form:

$$J = A(1 - \bar{r}_v)T^2 exp(-e\phi/k_BT) \tag{B.7}$$

For clean surfaces, the reflection coefficient, $\bar{r}_v$, is small and insensitive to temperature. Therefore, the expression becomes:

$$J = AT^2 exp(-e\phi/k_BT) \tag{B.8}$$

APPENDIX C: DERIVATION OF ION RADIAL DIFFUSION EQUATION

In the orifice region, most of the ions generated are lost to the orifice walls. Therefore, considering that the ion production rate is equal to diffusion rate, the following expression can be written:

$$-\nabla \cdot [D_a \nabla n] = \dot{n} \tag{C.1}$$

where D_a is ambipolar diffusion coefficient and it is given by:

$$D_a = \frac{1}{\sigma_{cex}N} \frac{q}{m_i} \left(\frac{T_i + T_e}{u_{scat}} \right) \tag{C.2}$$

where σ_{cex} is neutral-ion resonant charge exchange cross-section and u_{scat} is the scattering speed and it can be approximated as ion thermal speed for relatively small diffusion [37]:

$$u_{th} = \sqrt{\frac{qT_i}{m_i}} \tag{C.3}$$

The ion source term on the right hand side of Equation C.1 is given by:

$$\dot{n} = Nn\sigma\left(T_e\right) \sqrt{\frac{8qT_e}{\pi m_e}} \tag{C.4}$$

When we ignore the axial density gradients and radial variations of electron temperature and neutral particle density, ambipolar diffusion coefficient can be taken out. Since the Laplacian operator is defined as the divergence of the gradient of a function, Equation C.1 can be written as:

$$-D_a \nabla^2 n = \dot{n} \tag{C.5}$$

In expanded form:

$$-D_a \left[\frac{1}{r}\frac{\partial}{\partial r}\left(r\frac{\partial n}{\partial r}\right) + \frac{1}{r^2}\frac{\partial^2 n}{\partial \phi^2} + \frac{\partial^2 n}{\partial z^2}\right] = \dot{n} \qquad \text{(C.6)}$$

Considering a slab geometry for the sake of simplicity, the angular terms in Equation C.6 can be eliminated and the equation becomes:

$$-D_a \left[\frac{\partial^2 n}{\partial r^2} + \frac{1}{r}\frac{\partial n}{\partial r} + \frac{\partial^2 n}{\partial z^2}\right] = Nn\sigma\left(T_e\right)\sqrt{\frac{8qT_e}{\pi m_e}} \qquad \text{(C.7)}$$

After final arrangement, the equation can be put in a tidy form:

$$\frac{\partial^2 n}{\partial r^2} + \frac{1}{r}\frac{\partial n}{\partial r} + \frac{\partial^2 n}{\partial z^2} + C^2 n = 0 \qquad \text{(C.8)}$$

where

$$C^2 = \frac{N\sigma\left(T_e\right)\sqrt{8qT_e/\pi m_e}}{D_a} \qquad \text{(C.9)}$$

Equation C.1 can be solved by using separation of variables method. Considering that $n(r,z) = F(r)G(z)$, the partial derivatives of $n(r,z)$ are:

$$\begin{aligned} \frac{\partial n}{\partial r} &= F'G & \frac{\partial n}{\partial z} &= FG' \\ \frac{\partial^2 n}{\partial r^2} &= F''G & \frac{\partial^2 n}{\partial z^2} &= FG'' \end{aligned} \qquad \text{(C.10)}$$

Plugging this derivatives into Equation C.8 and making necessary arrangements, we obtain:

$$F''G + \frac{1}{r}F'G + C^2 FG = -FG'' \qquad \text{(C.11)}$$

Dividing both sides by FG, we end up with:

$$\frac{1}{F}\frac{\partial^2 F}{\partial r^2} + \frac{1}{rF}\frac{\partial F}{\partial r} + C^2 = -\frac{1}{G}\frac{\partial^2 G}{\partial z^2} \qquad \text{(C.12)}$$

The solution of left hand-side of Equation C.12 is the zeroth order Bessel function and the solution of right hand-side of Equation C.12 is an exponential function. Therefore, the solution of Equation C.8 is the product of these two.

$$n(r, z) = A J_0 \left(\sqrt{C^2 + \alpha^2} r \right) e^{-\alpha z} \tag{C.13}$$

where A is an arbitrary constant. At the origin, A is equal to $n(0,0)$. Hence, solution becomes:

$$n(r, z) = n(0,0) J_0 \left(\sqrt{C^2 + \alpha^2} r \right) e^{-\alpha z} \tag{C.14}$$

Assuming that the ion density is zero at the wall ($n(R, z) = 0$):

$$\sqrt{C^2 + \alpha^2} = \frac{\lambda_{01}}{R} \tag{C.15}$$

where λ_{01} is the first zero of the zeroth order Bessel function of the first kind and R represents the radius. If we take $\alpha = 0$, this eigenvalue gives us:

$$\sqrt{C^2} = \frac{\lambda_{01}}{R} \implies C = \frac{\lambda_{01}}{R} \tag{C.16}$$

Plugging this C into Equation C.9, we have:

$$\left(\frac{\lambda_{01}}{R} \right)^2 = \frac{N \sigma(T_e) \sqrt{8 q T_e / \pi m_e}}{D_a} \tag{C.17}$$

Simply taking the reciprocal of both sides, we have:

$$\left(\frac{R}{\lambda_{01}} \right)^2 = \frac{D_a}{N \sigma(T_e) \sqrt{8 q T_e / \pi m_e}} \tag{C.18}$$

Making the final arrangements, we end up with the following expression:

$$\left(\frac{R}{\lambda_{01}} \right)^2 N \sigma(T_e) \sqrt{\frac{8 q T_e}{\pi m_e}} - D_a = 0 \tag{C.19}$$

Solution of this equation, which is only dependent on the electron temperature, gives the plasma electron temperature. As shown in study [37], axial ion density gradients in the orifice is small. Therefore, axial dependence of Equation C.1 disappears. In this case, using the same methodology explained above, the solution of the ion radial flow equation becomes only a zeroth order Bessel function (the solution does not have the exponential term). Following the solution steps, explained in detail above, gives us the same electron temperature equation.

APPENDIX D: ENERGY TAKEN AWAY FROM PLASMA DUE TO ELECTRONS STRIKING AN ANODE

In this section, the energy taken away form plasma with electrons being lost to an anode is derived. This derivation is of primary importance for calculating how much energy is transferred to the walls of the cathode (insert material and orifice wall) from the particles (electrons and ions) coming from plasma and recombining on the cathode wall. It is also important to calculate how much energy is taken away from plasma. It should be noted that the anode potential considered in this derivation is more negative than the plasma. The Maxwellian plasma electrons are slowed down by the sheath potential on the anode surface. The electron current density to the anode is given by [11]:

$$
\begin{aligned}
J_r = qn_e \int_{-\infty}^{\infty} dv_x \int_{-\infty}^{\infty} dv_y \int_{\sqrt{2q\phi_s/m_i}}^{\infty} v_z \left(\frac{m_i}{2\pi k_B T_e}\right)^{\frac{3}{2}} exp\left(\frac{-m_i\left(v_x^2 + v_y^2 + v_z^2\right)}{2k_B T_e}\right) dv_z \\
= \frac{1}{4}qn_e\sqrt{\frac{8k_B T_e}{\pi m_i}}exp\left(-\frac{q\phi_s}{k_B T_e}\right)
\end{aligned}
\tag{D.1}
$$

Since the sheath potential is a retarding potential for electrons, the electrons must overcome this sheath potential to reach the wall. Therefore, the electron speed, assuming in the z-direction, must be at least $\sqrt{2q\phi_s/m_i}$. The Maxwellian plasma electrons lose their energy while they are passing through this sheath region. The power flux from plasma is given by:

$$
\begin{aligned}
P_e = n_e \int_{-\infty}^{\infty} dv_x \int_{-\infty}^{\infty} dv_y \int_{\sqrt{2q\phi_s/m_i}}^{\infty} v_z \left(\frac{m_e\left(v_x^2 + v_y^2 + v_z^2\right)}{2}\right) \left(\frac{m_i}{2\pi k_B T_e}\right)^{\frac{3}{2}} \\
exp\left(\frac{-m_i\left(v_x^2 + v_y^2 + v_z^2\right)}{2k_B T_e}\right) dv_z \\
= \frac{1}{4}qn_e\sqrt{\frac{8k_B T_e}{\pi m_i}}\left(2\frac{k_B T_e}{q} + \phi_s\right)exp\left(-\frac{q\phi_s}{k_B T_e}\right)
\end{aligned}
\tag{D.2}
$$

where ϕ_s represents the sheath potential in eV. Taking the ratio of the power per electron to the electron flux, the energy that an electron removes from the plasma in eV is:

$$E = \frac{P_e}{J_r} = 2\frac{k_B T_e}{q} + \phi_s = 2T_{eV} + \phi_s \tag{D.3}$$

where T_{eV} represents the electron temperature in eV. The energy that an electron transfers to the wall is different than the one that an electron removes from the plasma. As we mentioned above, the electrons lose their kinetic energy when they are passing through the sheath region. Therefore, $q\phi_s$ term needs be included in the electron particle energy expression. The power flux to the anode wall from Maxwellian plasma electrons can be calculated as follows:

$$P_e = n_e \int_{-\infty}^{\infty} dv_x \int_{-\infty}^{\infty} dv_y \int_{\sqrt{2q\phi_s/m_i}}^{\infty} v_z \left(\frac{m_e \left(v_x^2 + v_y^2 + v_z^2\right)}{2} - q\phi_s \right) \left(\frac{m_i}{2\pi k_B T_e} \right)^{\frac{3}{2}}$$

$$exp\left(\frac{-m_i \left(v_x^2 + v_y^2 + v_z^2\right)}{2k_B T_e} \right) dv_z$$

$$= \frac{1}{4} q n_e \sqrt{\frac{8k_B T_e}{\pi m_i}} \left(2\frac{k_B T_e}{q} \right) exp\left(-\frac{q\phi_s}{k_B T_e} \right)$$

$$\tag{D.4}$$

The energy transferred to the anode wall per electron can be calculated by taking the ratio of the power to the electron flux. Notice that the electron flux to the wall is the same as given above.

$$E = \frac{P_e}{J_r} = 2\frac{k_B T_e}{q} = 2T_{eV} \tag{D.5}$$

APPENDIX E: PUBLICATIONS PRODUCED FROM THIS RESEARCH

The list of publications produced from this thesis are listed below:

Journal Publications

(i) Korkmaz, O., M. Celik, "Global Numerical Model for the Assessment of the Effect of Geometry and Operation Conditions on Insert and Orifice Region Plasmas of a Thermionic Hollow Cathode Electron Source," Contributions to Plasma Physics, Vol. 54, No. 10, pp. 838-850, 2014.

International Conference Proceedings

(i) Korkmaz, O., M. Celik, "Global Numerical Model For Orifice and Insert Region of a Lanthanum Hexaboride Thermionic Hollow Cathode," 4th Space Propulsion Conference, Cologne, Germany, May 2014.

(ii) Ozturk, A. E., O. Korkmaz, M. Celik, "Design and Analysis of Different Insert Region Heaters of a Lanthanum Hexaboride Hollow Cathode During Initial Heating," 4th Space Propulsion Conference, Cologne, Germany, May 2014.

National Conference Proceedings

(i) Korkmaz, O., A. E. Öztürk, M. Çelik, "Elektrik İtki Sistemlerinde Elektron Kaynağı Olarak Kullanılmak Üzere Üretilen Oyuk Katodun Tasarım Süreci," *V.* Ulusal Havacılık ve Uzay Konferansı, Erciyes Üniversitesi, Kayseri, Türkiye, Eylül 2014.

REFERENCES

1. Criado, E., E. Roibás, S. P. Tierno, P. R. D. Francisco, J. L. Domenech-Garret, J. M. Donoso, and L. Conde, "Ion Beam Neutralization and Properties of Plasmas From Low Power Ring Cusp Ion Thrusters", *Physics of Plasmas*, Vol. 19, No. 2, p. 023505, 2012.

2. Roibás, E., S. P. Tierno, E. Criado, J. L. Doménech-Garret, J. J. M. Donoso, and L. Conde, "Characterization of the Ion Beam Neutralization of Plasma Thrusters Using Collecting and Emissive Langmuir Probes", *Contributions to Plasma Physics*, Vol. 53, No. 1, pp. 57–62, 2013.

3. Warner, D. J., "Advanced Cathodes For Next Generation Electric Propulsion Technology", M.Sc. Thesis, Air Force Institute of Technology, Dayton, OH, USA, 2008.

4. Goebel, D. M. and R. M. Watkins, "Compact Lanthanum Hexaboride Hollow Cathode", *Review of Scientific Instruments*, Vol. 81, No. 083504, 2010.

5. Warner, D. J., R. D. Branam, and W. A. Hargus, "Ignition and Plume Characteristics of Low-Current Cerium and Lanthanum Hexaboride Hollow Cathodes", *Journal of Propulsion and Power*, Vol. 26, No. 1, pp. 130–134, 2010.

6. Kuznetsov, G., "High Temperature Cathodes for High Current Density", *Nuclear Instruments and Methods in Physics Research Section A: Accelerators, Spectrometers, Detectors and Associated Equipment*, Vol. 340, No. 1, pp. 204–208, 1994.

7. Herniter, M. E. and W. D. Getty, "Thermionic Cathode Electron Gun for High Current Densities", *IEEE Transactions on Plasma Science*, Vol. PS-15, No. 4, pp. 351–360, 1987.

8. Broers, A. N., "Electron Gun using Long-Life Lanthanum Hexaboride Cathode", *Journal of Applied Physics*, Vol. 38, No. 4, pp. 1991–1992, 1967.

9. Courtney, D. G., "Development and Characterization of a Diverging Cusped Field Thruster and a Lanthanum Hexaboride Hollow Cathode", M.Sc. Thesis, Massachusetts Institute of Technology, Cambridge, MA, USA, 2008.

10. Trent, K. R., M. S. McDonald, R. B. Lobbia, and A. D. Gallimore, "Time-resolved Langmuir Probing of a New Lanthanum Hexaboride (LaB6) Hollow Cathode", 32nd *International Electric Propulsion Conference*, Weisbaden, Germany, September 2011, IEPC-2011-245.

11. Goebel, D. M. and I. Katz, *Fundamentals of Electric Propulsion: Ion and Hall Thrusters*, JPL Space Science and Technology Series, New York, USA, 2008.

12. Coletti, M., R. I. Marques, and S. B. Gabriel, "Discharge Hollow Cathode Design for a 4-Gridded Ion Engine", *IEEE Aerospace Conference*, pp. 1–12, IEEE, 2010.

13. Polk, J., A. Grubisic, N. Taheri, D. M. Goebel, R. Downey, and S. Hornbeck, "Emitter Temperature Distributions in the NSTAR Discharge Hollow Cathode", 41st *Joint Propulsion Conference*, Tucson, AZ, USA, July 2005, AIAA-2005-4398.

14. Goebel, D. M. and C. Emily, "High Current Lanthanum Hexaboride Hollow Cathodes for High Power Hall Thrusters", 32nd *International Electric Propulsion Conference*, Weisbaden, Germany, September 2011, IEPC-2011-053.

15. Goebel, D. M., J. T. Crow, and A. T. Forrester, "Lanthanum Hexaboride Hollow Cathode for Dense Plasma Production", *Review of Scientific Instruments*, Vol. 49, No. 4, pp. 469–472, 2008.

16. Lafferty, J. M., "Boride Cathodes", *Journal of Applied Cathodes*, Vol. 22, No. 3, 1951.

17. Storms, E. K. and B. A. Muller, "A study of Surface Stoichiometry and Thermionic Emission Using LaB6", *Journal of Applied Physics*, Vol. 50, No. 5, pp. 3691 – 3698,

1979.

18. Jacobson, D. L. and E. K. Storms, "Work Function Measurement of Lanthanum - Boron Compounds", *IEEE Transactions on Plasma Science*, Vol. 6, No. 2, pp. 191 – 199, 1978.

19. Kim, V., G. Popov, B. Arkhipov, V. Murashko, A. Koroteyev, V. Garkusha, A. Semenkin, and S. Tverdokhlebov, "Electric Propulsion Activity in Russia", 27th *International Electric Propulsion Conference*, Pasadena, CA, USA, October 2001, IEPC-2001-005.

20. Arkhopov, B. A. and K. N. Kozubsky, "The Development of the Cathode Compensators for Stationary Plasma Thrusters in the USSR", 22nd *International Electric Propulsion Conference*, Viareggio, Italy, October 1991, IEPC-91-023.

21. Storms, E. K. and B. A. Muller, "Phase Relationship, Vaporization, and Thermodynamic Properties of the Lanthanum-Boron System", *The Journal of Physical Chemistry*, Vol. 82, No. 1, pp. 51 – 59, 1978.

22. Goebel, D. M., Y. Hirooka, and T. Sketchley, "Large Area Lanthanum Hexaboride Electron Emitter", *Review of Scientific Instruments*, Vol. 56, pp. 1717 – 1722, 1985.

23. Favreau, L. J., "Cataphoretic Coating Lanthanum Boride on Rhenium Filaments", *Review of Scientific Instruments*, Vol. 36, pp. 856 – 857, 1965.

24. Pelletier, J. and C. Pomot, "Work Function of Sintered Lanthanum Hexaboride", *Applied Physics Letters*, Vol. 34, No. 4, pp. 249 – 251, 1979.

25. Storms, E. K., "Thermionic Emission and Vaporization Behavior of the Ternary Systems of Lanthanum Hexaboride Containing Molybdenum Boride, Molybdenum Diboride, Zirconium Diboride, Gadolinium Hexaboride, and Neodymium Hexaboride", *Journal of Applied Physics*, Vol. 54, No. 2, pp. 1076 – 1081, 1983.

26. Goebel, D. M., R. M. Watkins, and K. Jameson, "LaB_6 Hollow Cathodes for Ion and Hall Thrusters", *Journal of Propulsion and Power*, Vol. 23, No. 3, pp. 527 – 528, 2010.

27. Warner, D. J., R. D. Branam, W. A. Hargus, and D. M. Goebel, "Low Current Cerium Hexaboride and Lanthanum Hexaboride Hollow Cathodes", 46th *AIAA Aerospace Sciences Meeting and Exhibit*, Reno, NV, USA, January 2008, AIAA-2008-1086.

28. Falce, L., "Dispenser cathodes: The Current State of the Technology", *International Electron Devices Meeting*, Vol. 29, pp. 448–451, IEEE, 1983.

29. Ives, R. L., L. R. Falce, S. Schwartzkopf, and R. Witherspoon, "Controlled Porosity Cathodes From Sintered Tungsten Wires", *IEEE Transactions on Electron Devices*, Vol. 52, No. 12, pp. 2800–2805, 2005.

30. Levi, R., "Improved Impregnated Cathode", *Journal of Applied Physics*, Vol. 26, No. 5, pp. 639–639, 2004.

31. Cronin, J. L., "Modern Dispenser Cathodes", *IEE Proceedings I (Solid-State and Electron Devices)*, Vol. 128, No. 1, pp. 19–32, 1981.

32. Kovaleski, S. D., "Life Model of Hollow Cathodes Using a Barium Calcium Aluminate Impregnated Tungsten Emitter", 27th *International Electric Propulsion Conference*, Pasadena, CA, USA, October 2001, IEPC-01-276.

33. Polk, J. E., D. M. Goebel, and R. Watkins, "Characterization of Hollow Cathode Performance and Thermal Behaviour", 42nd *Joint Propulsion Conference*, Sacramento, CA, USA, July 2006, AIAA-2006-5150.

34. Domonkos, M. T., "Evaluation of Low-Current Orificed Hollow Cathodes", Ph.D. Thesis, The University of Michigan, Ann Arbor, MI, 1999.

35. Mikellides, I. G., I. Katz, D. M. Goebel, J. E. Polk, and K. K. Jameson, "Plasma Processes Inside Dispenser Hollow Cathodes", *Physics of Plasmas*, Vol. 13, No. 6, p. 063504, 2006.

36. Mandell, M. J. and I. Katz, "Theory of Hollow Cathode Operation in Spot and Plume Modes", 30th *Joint Propulsion Conference*, Indianapolis, IN, USA, June 1994, AIAA-94-3134.

37. Katz, I., J. R. Anderson, J. E. Polk, and J. R. Brophy, "One-Dimensional Hollow Cathode Model", *Journal of Propulsion and Power*, Vol. 19, No. 4, pp. 595–600, 2003.

38. Mikellides, I. G., I. Katz, D. M. Goebel, and J. E. Polk, "Hollow Cathode Theory and Experiment. II. A Two-dimensinal Theoretical Model of the Emitter Region", *Journal of Applied Physics*, Vol. 98, No. 113303, 2005.

39. Mikellides, I. G., I. Katz, D. M. Goebel, and K. K. Jameson, "Evidence of Non-classical Plasma Transport in Hollow Cathodes for Electric Propulsion", *Journal of Applied Physics*, Vol. 101, No. 6, p. 063301, 2007.

40. Albertoni, R., M. Andrenucci, D. Pedrini, and F. Paganucci, "Preliminary Characterization of a LaB_6 Hollow Cathode for Low Power Hall Effect Thrusters", 33rd *International Electric Propulsion Conference*, Washington, DC, USA, October 2013, IEPC-2013-137.

41. Fossum, E. C., J. D. Sommerville, and L. B. King, "Characterization of Near Field Plasma Environment of a Hollow Cathode Assembly", 40th *Joint Propulsion Conference*, Fort Lauderdale, FL, USA, July 2004, AIAA-2004-3795.

42. Domonkos, M. T., M. J. Patterson, and A. D. Gallimore, "Low-current, Xenon Orificed Hollow Cathode Performance for In-Space Applications", *Journal of Propulsion and Power*, Vol. 19, No. 3, pp. 438–443, 2003.

43. Katz, I., M. J. Mandell, M. Patterson, and M. Domonkos, "Sensitivity of Hollow Cathode Performance to Design and Operating Parameters", 35th *Joint Propulsion Conference*, Los Angeles, CA, USA, June 1999, AIAA-99-2576.

44. Mizrahi, J., V. Vekselman, V. Gurovich, and Y. E. Krasik, "Simulation of Plasma Parameters During Hollow Cathodes Operation", *Journal of Propulsion and Power*, Vol. 28, No. 5, pp. 1134–1137, 2012.

45. Albertoni, R., D. Pedrini, F. Paganucci, and M. Andrenucci, "A Reduced Order Model For Thermionic Hollow Cathodes", *IEEE Transactions on Plasma Science*, Vol. 43, No. 7, pp. 1731–1745, 2013.

46. Mikellides, I. G. and I. Katz, "Wear Mechanisms in Electron Sources for Ion Propulsion, 1: Neutralizer Hollow Cathode", *Journal of Propulsion and Power*, Vol. 24, No. 4, pp. 855–865, 2008.

47. Mikellides, I. G., "Effects of Viscosity in a Partially Ionized Channel Flow With Thermionic Emission", *Physics of Plasma*, Vol. 16, No. 1, p. 013501, 2009.

48. Mikellides, I. G., D. M. Goebel, J. S. Snyder, I. Katz, and D. A. Herman, "The Discharge Plasma In Ion Engine Neutralizers: Numerical Simulations and Comparisons With Laboratory Data", *Journal of Applied Physics*, Vol. 108, No. 11, p. 113308, 2010.

49. Mikellides, I. G., I. Katz, D. M. Goebel, K. K. Jameson, and J. E. Polk, "Wear Mechanisms in Electron Sources for Ion Propulsion, II: Discharge Hollow Cathode", *Journal of Propulsion and Power*, Vol. 24, No. 4, pp. 866–879, 2008.

50. Katz, I., I. G. Mikellides, D. M. Goebel, and J. E. Polk, "Insert Heating and Ignition in Inert-Gas Hollow Cathodes", *IEEE Transactions on Plasma Science*, Vol. 36, No. 5, pp. 2199–2206, 2008.

51. Boyd, I. D. and M. W. Crofton, "Modelling the Plasma of a Hollow Cathode",

Journal of Applied Physics, Vol. 95, No. 7, pp. 3285–3296, 2004.

52. Levko, D., Y. E. Krasik, V. Vekselman, and I. Haber, "Two Dimensional Model of Orificed Micro Hollow Cathode Discharge For Space Application", *Physics of Plasmas*, Vol. 20, No. 8, p. 083512, 2013.

53. Crawford, F. W. and I. L. Freeston, "The Double Sheath at a Discharge Constriction", 6th *International Conference on Ionization Phenomena in Gases*, Paris, July 1963, v.1 pp. 461-464.

54. Goebel, D. M., K. K. Jameson, R. M. Watkins, and I. Katz, "Hollow Cathode and Keeper-Region Plasma Measurements Using Ultra-Fast Miniature Scanning Probes", 40th *Joint Propulsion Conference*, Fort Lauderdale, FL, USA, July 2004, AIAA-2004-3430.

55. Malik, A. K., P. Montarde, and M. G. Haines, "Spectroscopic Measurements on Xenon Plasma in a Hollow Cathode", *Journal of Physics D: Applied Physics*, Vol. 33, No. 16, pp. 2037–2048, 2000.

56. Siegfried, D. E. and P. J. Wilbur, "A Model for Mercury Orificed Hollow Cathodes:Theory and Experiment", *AIAA Journal*, Vol. 22, No. 10, pp. 1405–1412, 1984.

57. Chu, E. and D. M. Goebel, "High-Current Lanthanum Hexaboride Hollow Cathode for 10-to-50-kW Hall Thrusters", *IEEE Transactions on Plasma Science*, Vol. 40, No. 9, pp. 2133–2144, 2012.

58. Domonkos, M. T., "A Particle and Energy Balance Model of the Orificed Hollow Cathode", 38th *Joint Propulsion Conference*, Indianapolis, IN, USA, July 2002, AIAA-2002-4240.

59. Tanaka, T., "The Thermal and Electrical Conductivities of LaB_6 at High Temperatures", *Journal of Physics C: Solid State Physics*, Vol. 7, No. 9, pp. L177–L180,

1974.

60. Incropera, F. P. and D. P. DeWitt, *Fundamentals of Heat and Mass Transfer*, New York, USA: John Wiley & Sons, 1996.

61. Capacci, M. and A. S. M. Minucci, "Simple Numerical Model Describing Discharge Parameters in Orificed Hollow Cathode Devices", 33rd *Joint Propulsion Conference*, Seattle, WA, USA, July 1997, AIAA-97-2791.

62. Siegfried, D. E. and P. J. Wilbur, "An Investigation of Mercury Hollow Cathode Phenomena", 13th *International Electric Propulsion Conference*, San Diego, CA, USA, April 1978, AIAA-78-705.

63. Salhi, A., "Theoretical and Experimental Studies of Orificed, Hollow Cathode Operation", Ph.D. Thesis, Ohio State University, Columbus, OH, USA, 1993.

64. Goebel, D. M., K. K. Jameson, and R. R. Hofer, "Hall Thruster Cathode Flow Impact on Coupling Voltage and Cathode Life", *Journal of Propulsion and Power*, Vol. 28, No. 2, pp. 355–363, 2012.

65. Jameson, K. K., D. M. Goebel, and R. M. Watkins, "Hollow Cathode and Thruster Discharge Chamber Plasma Measurements Using High-Speed Scanning Probes", 29th *International Electric Propulsion Conference*, Princeton, NJ, USA, October 2005, IEPC-2005-269.

66. Siegfried, D. E., "A Phenomenological Model for Orificed Hollow Cathodes", Ph.D. Thesis, Colorado State University, Fort Collins, CO, USA, 1992.

67. Polk, J., C. Marrese, B. Thornber, L. Dang, and L. Johnson, "Temperature Distributions in Hollow Cathode Emitters", 40th *Joint Propulsion Conference*, Fort Lauderdale, FL, USA, July 2004, AIAA-2004-4116.

68. Noord, J. L. V., H. Kamhawi, and H. K. McEwen, "Characterization of a High

Current, Long Life Hollow Cathode", 29th *International Electric Propulsion Conference*, Princeton, NJ, USA, October 2005, IEPC-2005-321.

69. Katz, I., I. G. Mikellides, J. E. Polk, D. M. Goebel, and S. E. Hornbeck, "Thermal Model of the Hollow Cathode Using Numerically Simulated Plasma Fluxes", *Journal of propulsion and power*, Vol. 23, No. 3, pp. 527–526, 2007.

70. Mikellides, I. G., I. Katz, D. M. Goebel, and J. E. Polk, "Theoretical Model of a Hollow Cathode Plasma for the Assessment of Insert and Keeper Lifetimes", 41st *Joint Propulsion Conference*, Tucson, AZ, USA, July 2005, AIAA-2005-4234.

71. Plasek, M. L., B. Jorns, E. Y. Choueiri, and J. E. Polk, "Exploration of RF-Controlled High Current Density Hollow Cathode Concepts", 48th *Joint Propulsion Conference*, Atlanta, GA, USA, July 2012, AIAA-2012-4083.

72. Herring, C. and M. H. Nichols, "Thermionic Emission", *Reviews of Modern Physics*, Vol. 21, No. 2, p. 185, 1949.